



# Coronal Electron Densities Derived with Images Acquired during the 2017 August 21 Total Solar Eclipse

A. Bemporad

Istituto Nazionale di Astrofisica (INAF), Osservatorio Astrofisico di Torino, via Osservatorio 20, I-10025 Pino Torinese, Torino, Italy; [alessandro.bemporad@inaf.it](mailto:alessandro.bemporad@inaf.it)  
Received 2020 October 12; revised 2020 October 22; accepted 2020 October 22; published 2020 December 3

## Abstract

The total solar eclipse of 2017 August 21 was observed with a digital single lens reflex (DSLR) camera equipped with a linear polarizing filter. A method was developed to combine images acquired with 15 different exposure times (from 1/4000 s to 4 s), identifying in each pixel the best interval of detector linearity. The resulting mosaic image of the solar corona extends up to more than 5 solar radii, with a projected pixel size of 3.7 arcsec/pixel and an effective image resolution of  $10''2$ , as determined with visible  $\alpha$ -Leo and  $\nu$ -Leo stars. Image analysis shows that in the inner corona the intensity gradients are so steep that nearby pixels show a relative intensity difference of up to  $\sim 10\%$ ; this implies that care must be taken when analyzing single exposures acquired with polarization cameras. Images acquired with two different orientations of the polarizer have been analyzed to derive the degree of linear polarization and the polarized brightness  $pB$  in the solar corona. After intercalibration with  $pB$  measurements by the K-Cor instrument on Mauna Loa Solar Observatory (MLSO), the data analysis provided the 2D coronal electron density distribution from 1.1 up to  $\sim 3$  solar radii. The absolute radiometric calibration was also performed with the full Sun image and with magnitudes of visible stars. The resulting absolute calibrations show a disagreement by a factor of  $\sim 2$  with respect to MLSO; interestingly, this is the same disagreement recently found with eclipse predictions provided by MHD numerical simulations.

*Unified Astronomy Thesaurus concepts:* Solar corona (1483); Ground-based astronomy (686); Solar eclipses (1489); Total eclipses (1704); Polarimetry (1278); Polarimeters (1277); Amateur astronomy (35); Amateur astronomers (34); Visual observation (1778); Coronagraphic imaging (313); CCD photometry (208); Photometry (1234)

## 1. Introduction

Despite the actual availability of coronagraphic data acquired by many ground-based and space-based instruments, the occurrence of total solar eclipses still offers today a unique opportunity to observe the full corona from almost the edge of the solar disk up to many solar radii, allowing one to test new instrumentation (e.g., Samra et al. 2018; Madsen et al. 2019), new ideas (Reginald et al. 2019) and complementing other observations (Pasachoff 2017). Moreover, these fascinating events offer at the same time the possibility of involving the general public in astrophysics in general and solar physics in particular.

Over the last  $\sim 15$  yr, the availability of standard digital single lens reflex (DSLR) cameras, coupled with personal computers and freeware astroimaging tools, has allowed an increasing number of people (scientists, amateur astronomers, teachers) not only to acquire high-quality astronomical observations but also to perform real scientific research. A nice example is given by the increasing number of papers analyzing these images to perform, for instance, stellar photometry (Hoot 2007; Kloppenborg et al. 2012; Pieri 2012; Zhang et al. 2016; Axelsen 2017). Thanks to the linearity of more recent CCDs mounted on DSLR cameras, it has been shown that these instruments can be used to characterize variable stars and novae (Fiacconi & Tinelli 2009; Collins & Prasai 2009; Loughney 2010; Banyś & Kata 2014; Deshmukh 2015; Walker et al. 2015; Pyatnytsky 2019; Nesci et al. 2020), even without the need for a telescope and a mount motor drive, and to observe the transits of exoplanets (Littlefield 2010; Miller 2015), eclipsing binary stars (Collins 2013; Richards et al. 2019), meteor spectral emissions (Cheng & Cheng 2011), and asteroid occultations (Hoot 2012), and even to build

color-magnitude diagrams of open clusters (Jang & Song 2015). Although these works are mostly addressed to amateur astronomers and educators, they also show that, even though not explicitly designed for scientific applications, DSLR cameras can nevertheless produce high-quality data with only a minimal investment of funds.

Surprisingly, the above list of published papers shows a very limited number of works doing research with DSLR cameras in solar physics, with the exception of a few recent works focusing on the measurement of plasma physical parameters in a quiescent prominence (Jejčić et al. 2014) based on the method of Jejčić & Heinzel (2009), the determination of contact times of solar eclipses and planetary transits across the solar disk (Di Giovanni 2016), the measurement of the apparent variations of the size of the Sun (Trillenber 2019), and the recent observations of the total solar eclipse (TSE) of 2017 August 21 (Pasachoff et al. 2018; Snik et al. 2020). In particular, the latter spectacular event was observed by thousands of people as the path of totality crossed the whole United States from coast to coast, and it allowed for the first time the involvement of the general public in vast citizen-science projects, for instance to observe cloud and temperature properties associated with the transit of the eclipse (Dodson et al. 2019), to measure the ionospheric response to the variable solar illumination (Frissell et al. 2018), to capture (with the “Citizen CATE Experiment”; Penn et al. 2020) a time sequence of white-light coronal observations with identical instruments over  $\sim 90$  minutes of totality, or to collect (with the “Eclipse Megamovie Project”; Hudson et al. 2011) all DSLR pictures of the solar eclipse acquired by people across the United States to create a movie showing the high-resolution coronal dynamics close to the limb (see Hudson et al. 2018; Peticolas et al. 2019, for first results).



**Figure 1.** Picture showing the equipment employed on 2017 August 21 to acquire the TSE observations analyzed here (see text); the picture shows the DSLR camera mounted on the tripod, connected to remote controllers, and covered by a white tissue to reduce as much as possible the overheating by solar illumination during the PSE.

Almost  $\sim 100$  research papers have been already published on the 2017 August 21 TSE, dealing with data acquired from the ground with professional instrumentation and equipment and studying many different aspects such as the occurrence of transient and dynamic events (e.g., Hanaoka et al. 2018; Boe et al. 2020; Filippov et al. 2020), spectroscopic emissions by the E- and F-corona (e.g., Pasachoff et al. 2018; Samra et al. 2018; Koutchmy et al. 2019; Judge et al. 2019), validation of MHD models (Nandy et al. 2018; Mikić et al. 2018; Lamy et al. 2019), and many other topics related not only to research on solar physics but also to the response of the Earth’s ionosphere and atmosphere (e.g., Reinisch et al. 2018). On the other hand, only a couple of works discussed the scientific research that can be conducted simply with DSLR cameras, to constrain the locations of fainter coronal structures (Pasachoff et al. 2018) and to measure the degree of linear polarization (Snik et al. 2020).

In this work, I demonstrate how images acquired during a TSE with a single basic DSLR camera equipped with a cost-effective neutral density (ND) filter and linear polarizer can be analyzed to derive not only beautiful high-resolution images of the corona, but also to calibrate the polarized emission and measure the coronal electron densities. After a first description of instrumentation and observations (Section 2), I will describe how the images have been analyzed, calibrated, and combined in mosaics (Section 3) and discuss some interesting results from the mosaics (Section 4). Then, I will focus on the analysis of images acquired with the linear polarizer (Section 5) and show how, after relative and absolute radiometric calibrations (Section 6), the coronal electron densities have been finally measured (Section 7). The results are then summarized (Section 8).

## 2. Instrumentation and Observations

A preliminary description of the observational campaign is provided in Bemporad et al. (2017). The images were acquired near Idaho Falls, Idaho, in a location where the expected duration of totality was 2 minutes and 18 seconds; local seeing was almost perfect, with no visible clouds of any kind over the whole sky. The observations (Figure 1) were performed with a Canon EOS 1100D DSLR camera equipped with an EF 75–300 mm, f/4–5.6 III telephoto zoom lens and mounted on a fixed tripod (alto-azimuthal mount, no tracking); both the partial and total solar eclipse phases have been observed. In

particular, the two partial solar eclipse (PSE) phases (both before and after the totality) were fully covered by using a Baader OD5.0 solar filter (mounted on a sunshade) and setting the exposure time  $t_{exp}$  to  $1/4000$  s, with f/5.6 and ISO 100 sensitivity. The camera was first hand-focused at the maximum available focal length (300 mm) by looking at the edge of the Sun and also at the few small sunspots that were visible on the disk; the same focus was then employed for both the PSE and TSE phase observations.

With the help of a programmable LCD digital timer remote control, exposures were acquired at a time step of 68 s from the beginning of the PSE (first Moon contact C1) to 2 minutes and 45 s before the beginning of the TSE (second Moon contact C2); then the time step was increased to 3 s from C2 to the beginning of the TSE. The reason for this was to measure the shape of the PSE illumination curve as a function of time from C1 to C2 to test the theoretical curve for penumbra illumination level as derived for the ESA PROBA3 project (see Bemporad et al. 2015). Results from the analysis of these images (and those acquired from the end of the TSE at Moon contact C3 to the end of the PSE at Moon contact C4) will be described in a future publication.

At the beginning of TSE, the OD5.0 filter was quickly dismantled, and a first set of TSE exposures was acquired. In particular, autobracketing was performed by connecting the DSLR camera to a tablet running a freeware DSLR controller application. A first sequence of 15 exposures (with 15 different exposure times going from  $t_{exp} = 1/4000$  s up to  $t_{exp} = 4$  s; see Figure 6) was acquired, requiring a total acquisition time of about 35 s for the whole sequence. Then, a linear polarizer filter (Hoya 58 mm B58PLGB) was mounted in front of the zoom and (after verification of the orientation of the linear polarizer with respect to a reference mark) a second sequence of 15 exposures was acquired. The orientation of the linear polarizer was rotated clockwise by  $\sim 90^\circ$ , and a third sequence of 15 exposures was acquired again. Finally, after a further counter-clockwise rotation of the polarizer by  $\sim 45^\circ$ , a fourth and last sequence was acquired. Between each polarized sequence, the orientation of the linear polarizer was rotated by moving a reference arrow with respect to grooves on the rotating part of the filter mount (marked before the observational campaign) and separated by the right angular distances. At the end of the TSE, the linear polarizer was dismantled, and the OD5.0 filter was mounted again, starting the acquisition of the second PSE sequence first with a time step of 3 s, and then with a time step of 68 s to the end of the PSE.

At the end of the observations, three sequences of 15 dark frames were acquired by covering the zoom with the cap and by employing exactly the same  $t_{exp}$  used to acquire the bracketing sequence during the TSE. The same was also repeated for flat-field images, which were acquired by covering the lens with a uniform white fabric and pointing the camera at the sky.

## 3. From Image Sequences to Mosaics

The first step in the analysis of images acquired with a DSLR camera is the conversion from the RAW files to another format that is readable for the analysis by any programming language. In particular, in this work, the images have been converted from RAW to TIFF format with the open source program [DCRAW](#) freely distributed online. For the rest of the analysis described here, all of the routines have been written in

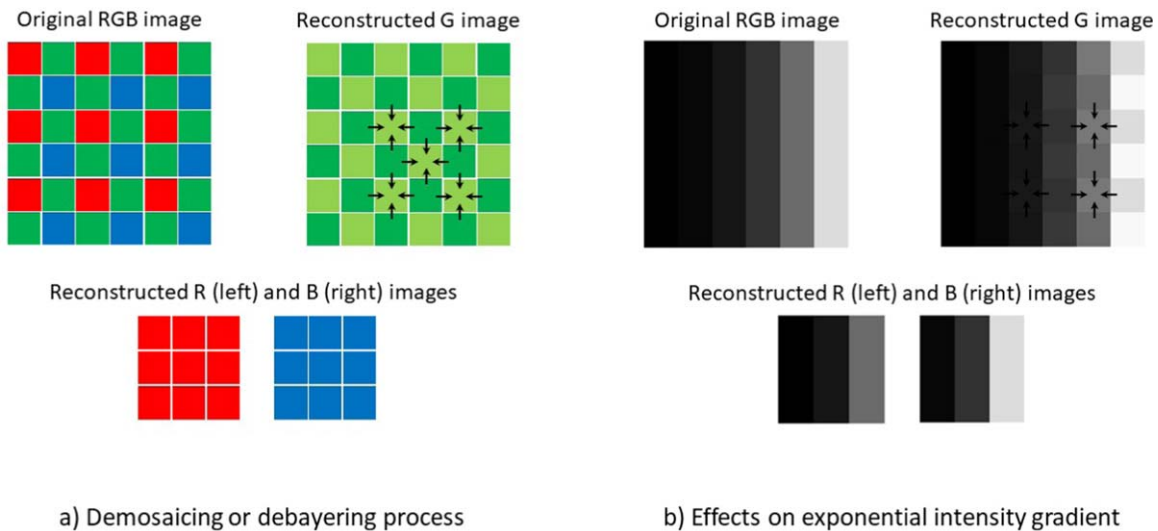


**Figure 2.** Panel (a): schematic representation of the methods followed to reconstruct from the original RGB image (top left) acquired with the RGB Bayer filter the three images in the G (top right), R, and B channels (bottom right); black arrows indicate the averaging performed among nearby green pixels to reconstruct the whole G image at full resolution. Panel (b): effects of the applied methods by assuming a uniform left–right exponential intensity gradient in the original image (top left), and the gradient in the resulting images (right); notice the systematic difference between the intensities of reconstructed R and B images.

Interactive Data Language (IDL), but any other open source programming language (such as Python or others) could be used.

### 3.1. Image Extraction

The second step in the analysis consists of the so-called demosaicking or debayering process (see, e.g., Páta et al. 2010): all DSLR cameras acquire images with a digital sensor overlaid with a color filter array (CFA), which is usually a Bayer filter alternating red (R) and green (G) filters for odd rows and green (G) and blue (B) filters for even rows (Figure 2). Because different filters (and hence different pixels) are integrating over different wavelength intervals, the intensity in each pixel also depends on the RGB color filter, and for the scientific analysis it is necessary to separate the three RGB colors. Hence, each TIFF image created from the RAW file (Figure 3) has been converted into three separate images for each one of the three RGB colors. The TIFF images have  $(4272 \times 2848)$  pixels, but with a Bayer filter, one-half of the pixels have a G filter, while one-quarter of the pixels have a B or an R filter (Figure 2). Hence, G images have been constructed with the same number  $(4272 \times 2848)$  of pixels by simple interpolation, by replacing the values in each R or B pixel with the average between the four nearby G pixels (black arrows in Figure 2, panel a). In contrast, R and B images have been constructed simply by reading the  $(2136 \times 1424)$  pixels with the R and B filters. This procedure has been applied not only to the images acquired during the PSE and TSE observations but also to the dark and flat-field images. The effects of these reconstruction methods on the coronal intensity gradients reconstructed in the three channels (Figure 2, panel b) will be discussed later.

### 3.2. Image Correction

Starting from the acquired dark and flat-field images, master images have been created, and all images have been corrected both for the dark currents and the flat field. The 2D distribution of flat-field intensities also provides correction for the

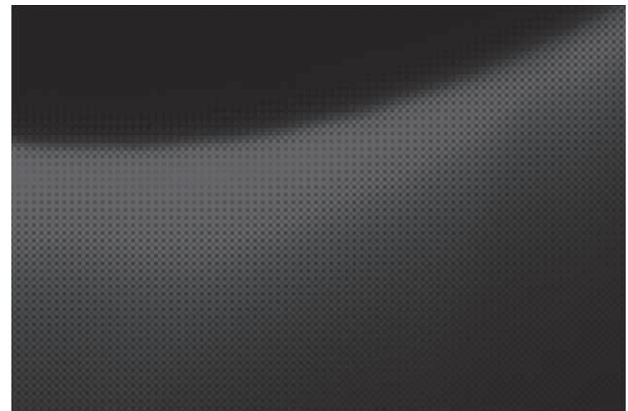


**Figure 3.** A zoom over the region near the edge of the occulting Moon in one of the RAW images acquired during the first TSE sequence; the image shows clearly the Bayer alternating pattern of RGB pixels.

vignetting of the optical system employed, which was not very important: the normalized flat-field images show center-to-corner relative intensity decreases of less than  $\approx 25\%$ . Because the tripod used was not motorized to follow the motion of the sky during the eclipse, image coalignment is required before combining the different exposures. This is a very important step, and the edge of the occulting disk of the Moon cannot be used as a reference for coalignment, because during the TSE the Moon is moving with respect to the Sun, and the images need to be coaligned with respect to the center of the Sun and not to the center of the Moon.

The easiest way to coalign different images is to use visible stars. In the G images, two brighter stars were clearly visible and were identified (by using the free open source program *Stellarium*): Regulus or  $\alpha$ -Leonis (apparent visual magnitude +1.35) and  $\nu$ -Leonis (apparent visual magnitude +5.15), located respectively bottom left and top right with respect to the Sun. The images have then been coaligned by using the positions of the brightest star Regulus determined in each frame. In the first sequence of 15 images acquired without the

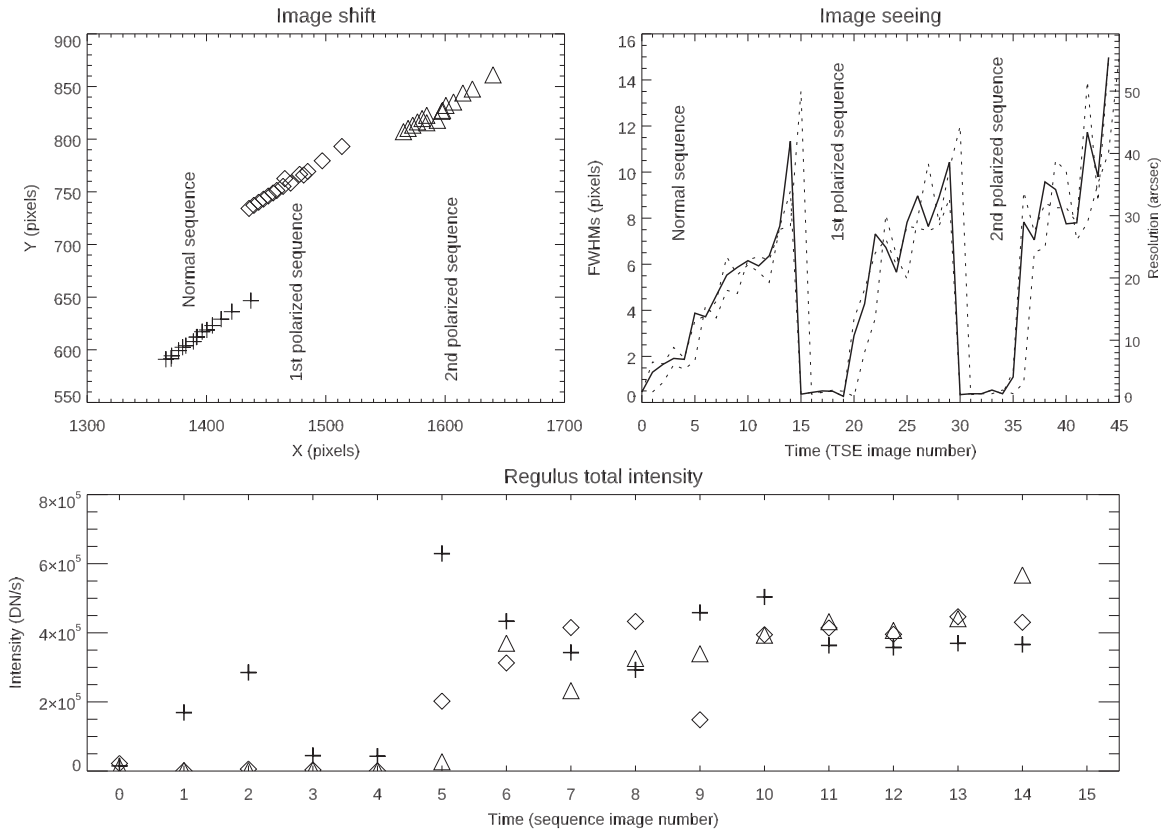


**Figure 4.** Top left: derived location (in pixels) of the Regulus star in each frame for the three acquired sequences (see text). Top right: corresponding FWHMs in the  $x$  and  $y$  directions (dotted lines) as derived from bidimensional Gaussian fitting, and the average FWHM (solid line) for the three image sequences. Bottom: corresponding total intensity [DN/s] normalized to the exposure time  $t_{exp}$  for the Regulus star for each image in the three sequences (symbols are the same used in the top left plot). Fluxes from polarized sequences have been multiplied by a factor of 4 to be comparable with those acquired without the polarizer.

polarizer, the star intensity is sufficiently high to identify its position in all of the frames acquired with  $t_{exp} > 1/60$  s. The positions of the star in the first frames were derived by back-extrapolating in time (with linear fitting) the position of the star derived with longer exposures. The results (top left panel in Figure 4) show that during the first sequence the star was displaced by about 90.3 pixels (in  $x$  and  $y$  directions). This displacement corresponds to  $334''.3$ , considering a pixel projected size of  $3.7$  arcsec/pix. Because the acquisition of the whole sequence of 15 exposures required about 35 s, this corresponds to an average motion of the sky of  $9.5$  arcsec/sec, corresponding to  $\sim 2.5$  pixels  $s^{-1}$ .

The above pixel projected size was determined from images acquired during the PSE: the Sun and Moon disks were fitted with circles, providing values of  $R_{Sun} = (257.7 \pm 0.2)$  pix and  $R_{Moon} = (267.0 \pm 0.2)$  pix for the projected radii of the Sun and the Moon. Because on 2017 August 21 the Sun was at a distance of 1.012 au from the Earth, the projected radius covered  $948.7$  arcsec, so the pixel size was  $948.7/257.7 = 3.7$  arcsec/pixel, corresponding to a two-pixel resolution of  $7''.4$ . The acquisition of the first five frames required only  $\sim 5$  s, so the expected motion of the star during the first five exposures was on the order of  $\sim 13$  pixels. The same method was applied to determine the position of the star Regulus during the first and second sequences acquired with the polarizer. Each sequence has been treated separately, because the application of the polarizing filter on the camera (between the first and second sequence) and the rotation of the filter (between the second and third sequence)

slightly changed the pointing of the camera, leading to the discontinuities visible in Figure 4 (top left panel).

The centroid position of the star in each frame was determined with bidimensional Gaussian fitting, and this also provided an estimate of the effective image resolution (given mainly by the combination of local seeing and the point-spread function (PSF) of the optical system). The resulting values of FWHMs for each one of the three sequences are shown in Figure 4 (top right panel). Because of the motion of the sky during the acquisition times, the measured FWHMs increase as  $t_{exp}$  becomes longer in each sequence; hence, a reference value is provided by the FWHM measured in the image acquired with the longer  $t_{exp}$  (to have a better signal-to-noise ratio) but still smaller than the time required for the star to move significantly in the image, for instance by more than one-quarter of a pixel ( $\sim 0.1$  s). This corresponds to the image acquired with  $t_{exp} = 1/16$  s: from this image the measured FWHM of Regulus turns out to be 5.52 pixels (hence HWHM of 2.76 pixels), corresponding to an effective image resolution (seeing plus PSF) of  $10''.2$ . Images acquired with longer exposure times were affected by blurring that is due to the motion of the sky, with higher effective resolutions shown in Figure 4 (top right panel).

The bidimensional Gaussian fitting of Regulus also provides an estimate of the total intensity  $I_{G,\alpha}$  in the G channel normalized for the exposure time (DN/s). In particular, the intensities measured for all exposures acquired in the three sequences are shown in Figure 4 (bottom panel), where the values measured with the polarizer (diamond and triangle

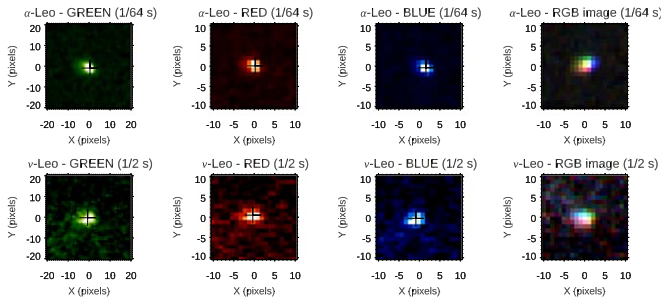


**Figure 5.** A zoom over the intensity distributions of the  $\alpha$ -Leonis (top row) and  $\nu$ -Leonis (bottom row) stars as obtained from the G (left), R (middle left), and B (middle right) channels, and the resulting RGB combined images (right panels) showing the chromatic aberrations of the optical system. Plus symbols show the centroid location of the intensity distribution for each color.

symbols) have been multiplied by a factor of 4 to be comparable with the values measured without the polarizer (plus symbols). The resulting intensities measured with the G images are almost constant for different exposure times, and the intensity is on average  $I_{G,\alpha} = (3.64 \pm 0.05) \times 10^5$  DN/s. This means that (at least for Regulus, which is a relatively weak source if compared with the much brighter inner solar corona) the linearity of the detector response is good, a characteristic that is very important for combining all of the exposures, as explained below.

Moreover, the 2D distributions of stellar intensities in the different colors also provide useful information on the possible optical aberrations (such as distortions and chromatic aberrations) introduced by the optical system. These effects can be quantified for the two visible stars  $\alpha$ -Leonis and  $\nu$ -Leonis, which were observed at distances from the image center (and hence from the optical axis) on the order of  $\sim 990$  pixels and  $\sim 1480$  pixels, respectively, quite far from the center of the field of view. In particular, Figure 5 shows the intensity distributions of  $\alpha$ -Leonis and  $\nu$ -Leonis in different colors as obtained with single exposures acquired with exposure times of 1/64 and 1/2 s. The results from bidimensional Gaussian fittings show that the 2D distributions of intensities have ratios between the Gaussian widths along the  $x$  and  $y$  directions of  $\sigma_x/\sigma_y \simeq 1.1$  for  $\alpha$ -Leonis and  $\simeq 1.3$  for  $\nu$ -Leonis. Figure 5 shows that the optical system employed spreads the point light sources as if rotated about the center of the image, what is called sagittal astigmatism. On the other hand, the centroid locations of stellar emissions in the three colors (plus symbols in Figure 5) have relative shifts of less than one pixel, leading to a limited level of chromatic aberration, shown in the right panels in Figure 5. In summary, considering the effective image resolution given above (2.76 pixels), these aberrations will have only second-order effects, in particular for the inner corona that was observed close to the center of the field of view.

### 3.3. Image Combination

After image coalignment with Regulus, it is possible to combine different exposures (once normalized by the exposure times) to get the best possible mosaic image covering the whole visible corona from the edge of the occulting disk of the Moon to larger altitudes. In particular, all of the images acquired during the first bracketing sequence and after the coalignment are shown in Figure 6 for different exposures. The image sequence shows that with shorter exposure times (top rows) only the inner corona is visible and no signal is detected farther

from the Sun, while for longer exposure times (bottom rows) the outer corona becomes visible, but the inner corona is entirely saturated. This makes the combination of all images not a trivial process, as is explained here.

Once the images are normalized for the exposure times, for each pixel it is possible to plot the measured intensity for increasing exposure time. Pixels located in the inner corona have almost the same signal for shorter exposures (thanks to the linearity already shown with Regulus), while as the exposure time increases the signal saturates, and this means that after normalization for the exposure time the observed signal goes almost to zero. This behavior is clearly shown in the bottom right panel of Figure 7, showing the intensity (normalized to the exposure time) from different images in one pixel located at a projected heliocentric distance of  $1.1 R_{Sun}$ . On the other hand, pixels located in the outer corona have almost a negligible signal in the first images, and then the signal rises, becoming almost constant for longer exposure times in the linearity interval. This opposite behavior is shown in the bottom left panel of Figure 7, relative to the intensity measured in a pixel located at  $4 R_{Sun}$ . In pixels at intermediate altitudes, the intensity first rises, reaching almost a constant value, and then decreases (Figure 7, bottom middle panel relative to a pixel located at  $2 R_{Sun}$ ).

For these reasons, the combination of the acquired images has been performed by deriving for each pixel the average intensity measured over the maximum number of exposures in the interval of linearity, determined with linear fitting. The resulting measured intensities for the three example pixels are shown by dashed horizontal lines in the bottom panels of Figure 7. The final combined image has then been constructed by iterating over all pixels and by replacing in each pixel the average intensity measured in this way. The output mosaic image for the G channel is shown in the top panel of Figure 7; the same operations have been repeated also for the R and B channels, building two mosaics with half-resolution with respect to the mosaic in the G channel. Notice that the curves shown in the bottom panels of Figure 7 show again (much better than the bottom panel of Figure 4) the good linearity of the detector response for varying exposure times.

The same techniques described above have been applied also to coalign and combine all of the exposures acquired with the linear polarizer. The only difference was that (because with the polarizer the star intensity was reduced by about a factor of 4) the identification of the Regulus star position in shorter frames was harder, and was made again by back-extrapolating the position of the star derived in longer exposures. Also, among the three sequences acquired with three different orientations of the polarizer, images acquired with the third and last orientation (after rotation by  $\sim 45^\circ$ ) have not been analyzed in this work, because (due to the short duration of this TSE) as the acquisition of the third polarized sequence started, the illumination coming from the first fraction of the solar disk emerging behind the edge of the Moon at the end of the TSE affected a significant part of those images (see the full image sequence thumbnails shown in Bemporad et al. 2017). A possible analysis of these images for limited coronal regions will be investigated in the future.

In the end, all of the above operations provided as output one mosaic image for each one of the three RGB channels, and for each one of the first three image sequences: the first one (acquired without the polarizer), and the second and third ones

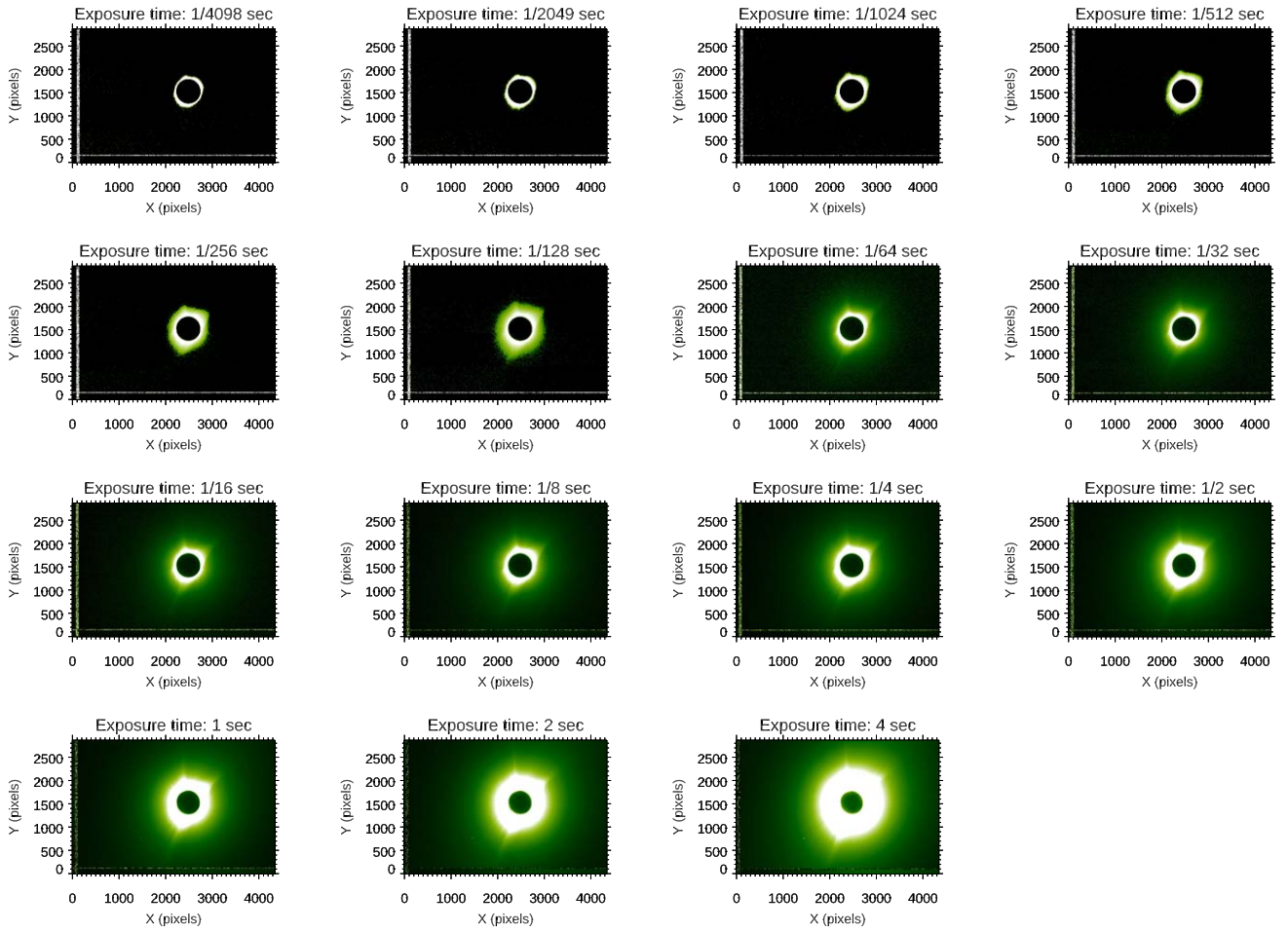


**Figure 6.** First bracketing sequence of 15 exposures (G channel) acquired without the linear polarizer, after the correction for dark currents and flat-fielding, demosaicking, coalignment, and normalization by the exposure times.

(acquired with two different orientations of the polarizer separated by  $90^\circ$ ). The scientific analysis of these images is described in the next sections.

## 4. Analysis of RGB Mosaics

### 4.1. RGB Intensity Distributions

Given the three mosaics in the RGB channels, one of the first interesting things to do is a direct comparison between the observed radial intensity profiles in the three channels. To this end, the higher-resolution G image has been interpolated to half of its resolution to become directly comparable with the R and B images. The comparison has been performed along four radial profiles, covering the projected heliocentric distances between  $1.05$  and  $3 R_{Sun}$ , and extracted along the central column (above (top) and below (bottom) the solar disk) and the central row (right and left with respect to the solar disk) passing through the disk center. The projected locations of pixels from which these profiles have been extracted are shown by yellow dotted lines in Figure 7; the resulting curves are given in Figure 8.

In particular, the left panels in this figure show the intensity profiles (DN/s) in the G channel extracted left and right (Figure 8, top left panel) and top and bottom (Figure 8, bottom left panel) with respect to the disk center. Notice that no smoothing has been applied to these curves that have been simply extracted along single columns and rows in the resulting

image mosaic: the low level of fluctuations shows the very good quality (i.e., good signal-to-noise ratio) obtained in this mosaic up to larger distances from the Sun. The other four panels in this figure show the relative difference (%) between R and G intensities (red solid lines) and between B and G intensities (blue solid lines) extracted left (top middle plot), right (top right plot), top (bottom middle plot), and bottom (bottom right plot) with respect to the disk center. These curves show clearly that in the inner corona (below  $\sim 1.5 R_{Sun}$ ) the intensities observed in the B channel are systematically higher than those in the R channel, but only in the left and top profiles, while in the right and bottom profiles the opposite occurs, with intensities in the R channel being systematically higher than those measured in the B channel. This means that these differences cannot be ascribed to different intensities in the bandpass of RGB filters, otherwise one should expect approximately the same behavior in the inner corona regardless of the latitudinal location in the corona. Also, this effect cannot be ascribed to chromatic aberrations, which would have the opposite effect of increasing the difference between the R and B intensities when going farther from the center of the field of view, and hence farther from the solar disk center.

Another explanation of this effect requires going back to the schematic representation given in Figure 2 (panel b); this figure clearly shows that, for instance in the hypothesis of an intensity decreasing uniformly only along image rows and from right to left (as occurs mainly in the intensity profiles extracted left with

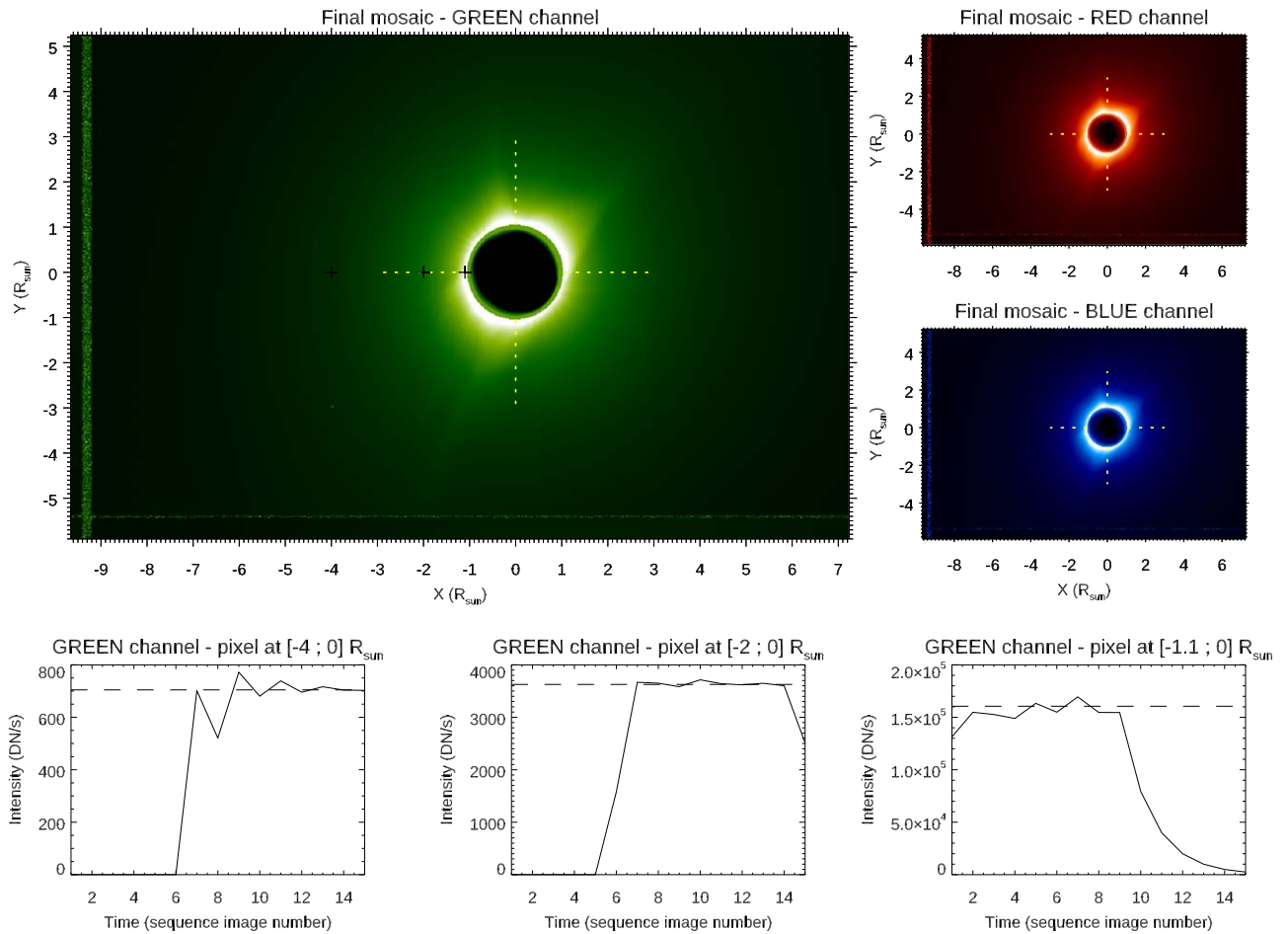


**Figure 7.** Top: resulting mosaic image in the G channel (top left) and in the B and R channels (top right) constructed from the sequence of 15 exposures. Bottom panels: intensity (DN/s) observed in three example pixels for different exposures. The locations of the three pixels are shown by the plus symbols in the top panel. The yellow dotted lines show the locations where RGB intensity profiles have been extracted to plot the panels of Figure 8.

respect to the solar disk), because in each RGB quadruplet the R pixels are always located at higher altitudes with respect to the B pixels, the reconstructed intensity profiles in the B channel are systematically higher than those reconstructed in the R channel. The opposite occurs considering what I called right profiles, where the R pixels are always located at lower altitudes with respect to the B pixels; a similar difference is present in the top profiles with respect to the bottom profiles. In summary, this means that the observed intensity differences between RGB pixels are mostly due to the different locations of those pixels. In particular, in the inner corona (below  $\sim 1.5 R_{Sun}$ ) the intensity radial gradients are so high that even the small difference in the projected altitude of nearby pixels (separated by  $3''7$ , corresponding to  $3.9 \times 10^{-3} R_{Sun}$ ) results in considerable relative intensity differences (up to  $\sim 5\%–10\%$ ).

This result has important implications that are discussed here. Over the last few years, different authors have demonstrated the advantages of using what is called a PolarCam or Polarization Imaging Camera to observe the solar corona (Reginald et al. 2017; Burkepile et al. 2017; Gopalswamy et al. 2018; Reginald et al. 2019; Judge et al. 2019; Fineschi et al. 2019; Vorobiev et al. 2020). This instrument consists of a camera (or a telescope, or any other optical system) equipped with a sensor having a micropolarizer array placed over the sensors (pixels) with four alternating orientations of linear polarizers. In practice, this is conceptually similar to a DSLR camera, where the four RGB

filters of the Bayer matrix (Figure 2, top left) are replaced with four linear micropolarizers. The obvious advantage of this camera is that the acquisition of a single exposure is sufficient to have in each superpixel four different measurements of the linear polarization at four different angles (0, 45, 90, and 135 degrees), allowing the optimal measurement of the total and polarized brightness of the corona and also high-cadence observations. Recently, the use of similar cameras has also been proposed as a payload of small satellites for solar coronagraphy from space (Gopalswamy & Gong 2018).

Nevertheless, the analysis of images acquired by a PolarCam is usually performed by assuming that the four subpixels in the same macropixel are sampling the same coronal plasma with four different orientations of the polarizer, and then reconstructing the four images corresponding to different polarizer orientations by simply collecting nearby pixels having the same micropolarizer orientation (e.g., Figure 2 by Reginald et al. 2017), without any interpolation to a common spatial grid. This working hypothesis is not always applicable, because each pixel is illuminated by a different coronal region, in principle. The problem is partially mitigated by the fact that the effective resolution is broadened by the instrument PSF and—for ground-based observations—also by the astronomical seeing. Nevertheless, Figure 8 shows that, even if these observations were acquired with a pixel projected size of 3.7 arcsec/pixel and an effective image resolution of 2.76 pixels, the intensity

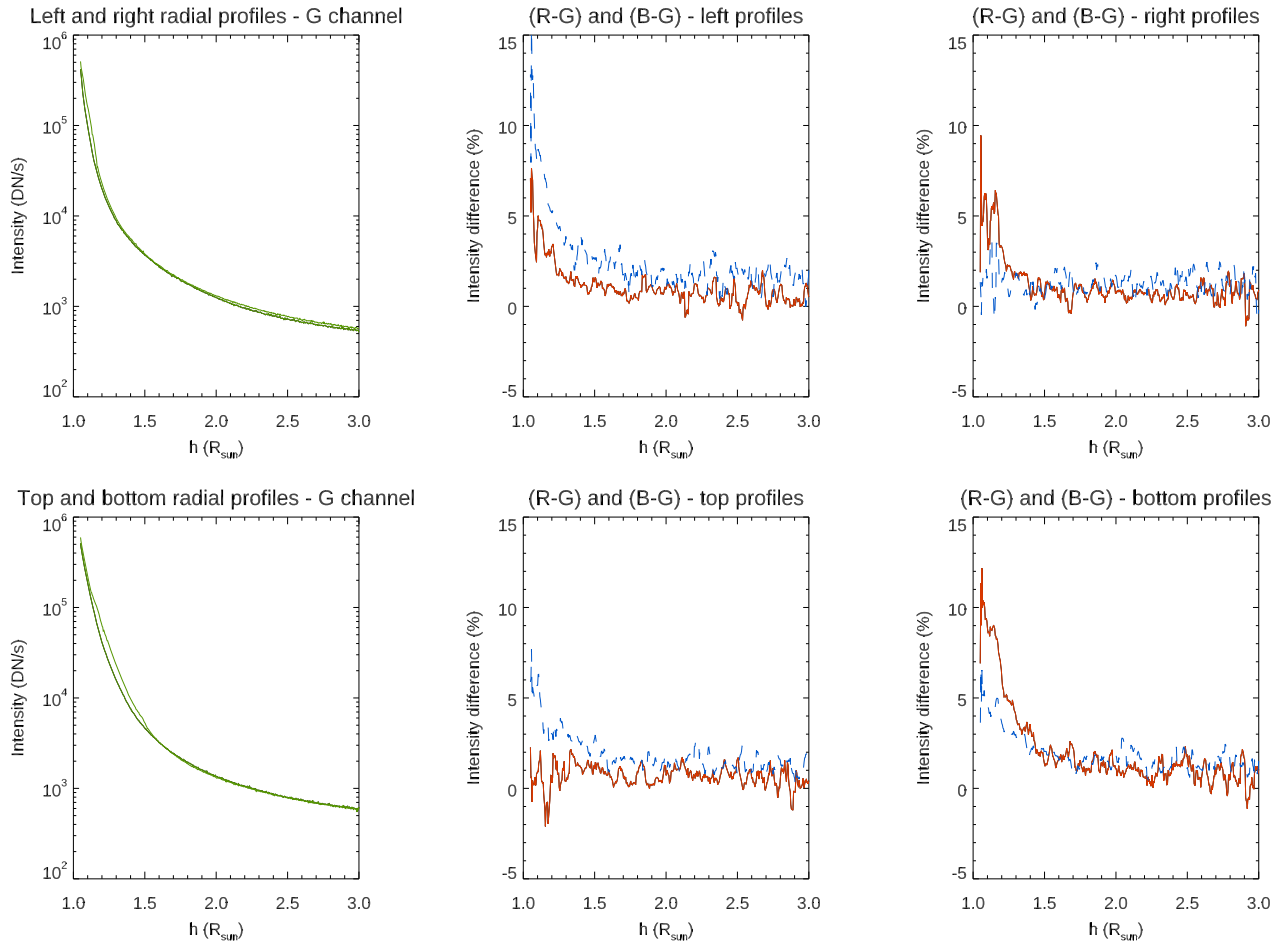


**Figure 8.** Left column: radial intensity (DN/s) profiles in the G channel plotted along the central row (top) and column (bottom) passing through the solar disk center as a function of heliocentric distance (yellow dotted lines in Figure 7). No smoothing has been applied to these curves. Middle and right columns: relative differences (%) between the R and G (solid red lines) and between the B and G (solid blue lines) intensity profiles extracted left (top middle panel), right (top right panel), top (bottom middle panel), and bottom (bottom right panel) with respect to the solar disk center (yellow dotted lines in Figure 7).

gradients in the inner corona are so steep that the different locations of RGB pixels result in different illumination levels. For a direct comparison, the PolarCam projected pixel sizes employed by Reginald et al. (2017), Judge et al. (2019), and Fineschi et al. (2019) were  $3''3$ ,  $2''87$ , and  $4''3$ , respectively, hence being comparable to or even larger than the projected pixel size of the DSLR camera employed in this work.

Thus, the main consequence of the plots shown in Figure 8 is that care must be taken in the analysis of data acquired with PolarCams in the inner regions of the solar corona (i.e., below  $1.5 R_{Sun}$ ): an error of up to  $\sim 10\%$  could be present in the derived measurements of total and polarized brightness, and hence in the electron density measurements.

#### 4.2. Image Filtering

One of the most interesting advantages of TSE observations is the possibility of observing not only large-scale but also smaller-scale and fainter features as density inhomogeneities expanding from very close to the solar limb. The observation of these features is very important, in particular because their orientation is usually believed to match the orientation of the coronal magnetic fields (see, e.g., Boe et al. 2020) that are dominating the dynamic of the coronal plasma but cannot be easily measured. In order to enhance the visibility of fainter coronal features in eclipse images, usually filtering methods are

required to flatten the strong radial intensity variations on the one hand, and also to increase the image contrast on the other hand. Many methods have been developed for these purposes over the last decades by different authors, such as the multidirectional maximum of second derivatives method (Koutchmy et al. 1988), the adaptive circular high-pass filter (ACHF) method (Druckmüller et al. 2006), the normalizing-radial-graded filter (NRGF) method (Morgan et al. 2006), the application of high-pass filters to improve signal-to-noise ratio (DeForest et al. 2018), and many other methods (see reviews by Pasachoff et al. 2007; Rušin et al. 2020, and references therein).

In this work, two simple combinations of standard mathematical methods were applied, methods that are freely available and distributed. The first one consists first of the application of the SOBEL filter (an edge-enhancement operator based on the detection of maximum image gradient directions), followed by a simple image smoothing to reduce the noise. The resulting image (Figure 9, left panel) plotted in log scale is quite similar to the natural appearance to the naked eye of the solar corona during TSE, and it shows not only the orientation of the main coronal features (such as coronal streamer and plumes) but also the location of the two visible stars: Regulus or  $\alpha$ -Leonis (close to the bottom left corner), and  $\nu$ -Leonis (close to the top right corner).

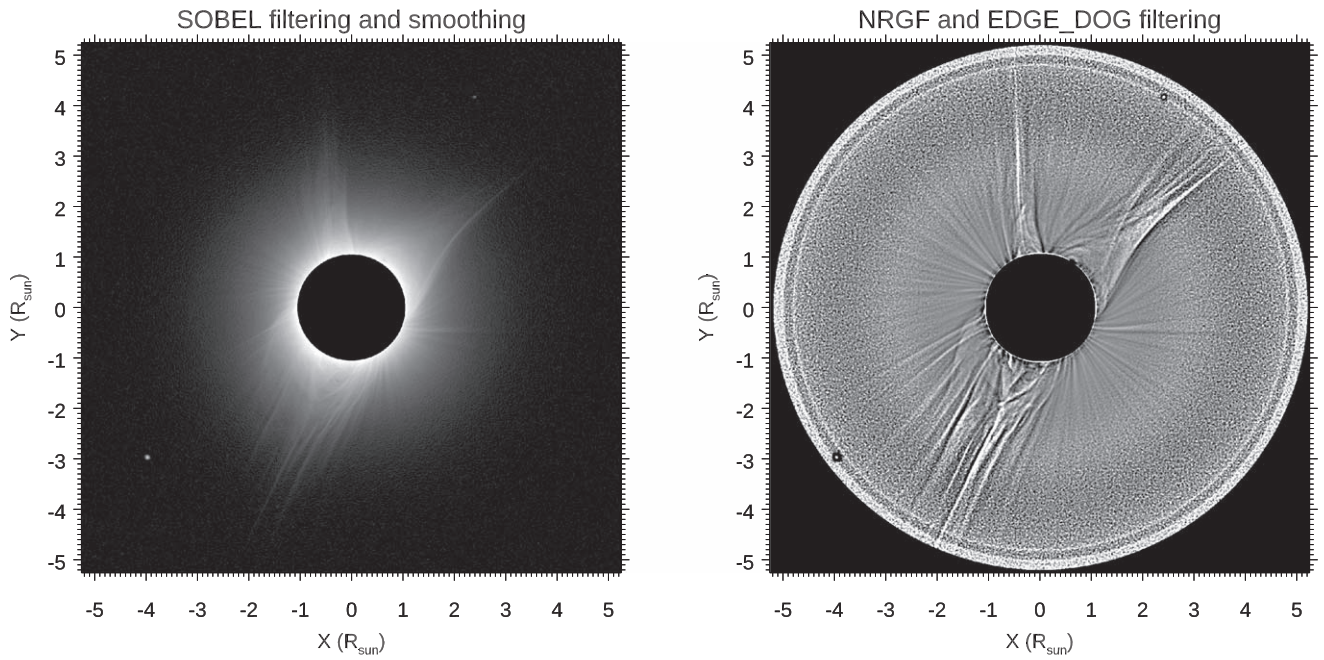


**Figure 9.** Left: image resulting from the mosaic in the G channel enhanced in contrast after application of the SOBEL filtering method and smoothing. Right: image resulting from the mosaic in the G channel enhanced in contrast after application of the NRGF and EDGE\_DOG filtering methods. Both images show also the  $\alpha$ -Leonis (close to the bottom left corner) and  $\nu$ -Leonis (close to the top right corner) stars.

The second combination consists of the application of the NRGF filter (freely distributed under SolarSoftware), followed by the so-called EDGE\_DOG filter (a bandpass filter based on the subtraction of two copies of the same image obtained after the application of different Gaussian blurrings). The resulting image (Figure 9, right panel) plotted in linear scale shows much better the outward extension of the fainter coronal features (plumes) that can be followed up to  $\sim 3 R_{Sun}$ , while brighter features (streamers) are visible up to the image edge located at  $\sim 5 R_{Sun}$ ; the  $\alpha$ -Leonis and  $\nu$ -Leonis stars are also clearly visible.

The filtered images can be used also to coalign the TSE observations with the solar north, based on images provided by other ground-based or space-based observatories. The determination of the rotation angle was performed here based on the calibrated total brightness image derived from the analysis of the polarized sequence, which is discussed below. Moreover, in this work the filtered images have been employed to derive the position of the center of the Sun behind the occulting lunar disk, given by the measured position of the visible stars and by the celestial coordinates of these stars and the Sun during TSE.

## 5. Analysis of Polarized Sequences

The mosaic images resulting from the combination of the two sequences of 15 exposures acquired with two different orientations of the linear polarizer (called Pol1 and Pol2, and separated by  $90^\circ$ ) are shown in Figure 10. The two images show, unfortunately, the presence of a ghost (due to unavoidable internal reflections from the linear polarizing filter); very similar features were also present, for instance, in images acquired by Snik et al. (2020; see their Figure 2). Because it is in principle unknown how the internal reflections from the filter modified the fraction of polarized emission from the corona, removal of these artifacts was not performed. In any case, these artifacts in the images affected only small, limited

regions of the observed corona, and their presence is clearly identifiable.

The relative difference between these two images (Figure 11, top left panel) clearly shows the so-called polarization cross, which is the cross-shaped distribution of pixels having almost a zero signal in the difference between the Pol1 and Pol2 images (plotted with white color in Figure 11, top left panel). The well-known existence of this polarization cross is related to the specific characteristics of the coronal emission which is linearly polarized. In general, the linear polarization is described by introducing the  $I$ ,  $Q$ , and  $U$  components of the Stokes vector  $S = [I, Q, U]$  representing the linearly polarized emission in each pixel  $(i, j)$ . In the simple case of no ellipticity of polarization (and hence no circular polarization), the  $Q$  and  $U$  components of the Stokes vector are given by

$$Q = I p \cos(2\alpha) \quad (1)$$

$$U = I p \sin(2\alpha) \quad (2)$$

where  $I$  [DN/s] is the total intensity,  $p = \sqrt{Q^2 + U^2}/I$  [%] is the degree of linear polarization, and  $\alpha$  is the angle of linear polarization, representing the angle of the direction of the electric field oscillation from a given plane. In the specific case of the solar K-corona emission (due to Thomson scattering of photospheric emission from free coronal electrons), the radiation has a partial linear polarization, and the orientation of the linear polarization vector is always tangent to the solar limb. This means that, for the position angles where  $\sin(2\alpha) = \cos(2\alpha)$ , the  $Q$  and  $U$  components are equal, and this happens for  $2\alpha = 45^\circ + k90^\circ$  ( $k = 0, 1, 2, 3$ ). Given the 2D intensity distributions  $I_{pol1}(i, j)$  and  $I_{pol2}(i, j)$  of the two images Pol1 and Pol2 acquired with the two different orientations of a linear polarizing filter separated by  $90^\circ$ , the distributions  $I(i, j)$ ,  $Q(i, j)$ , and  $U(i, j)$  of the Stokes vector

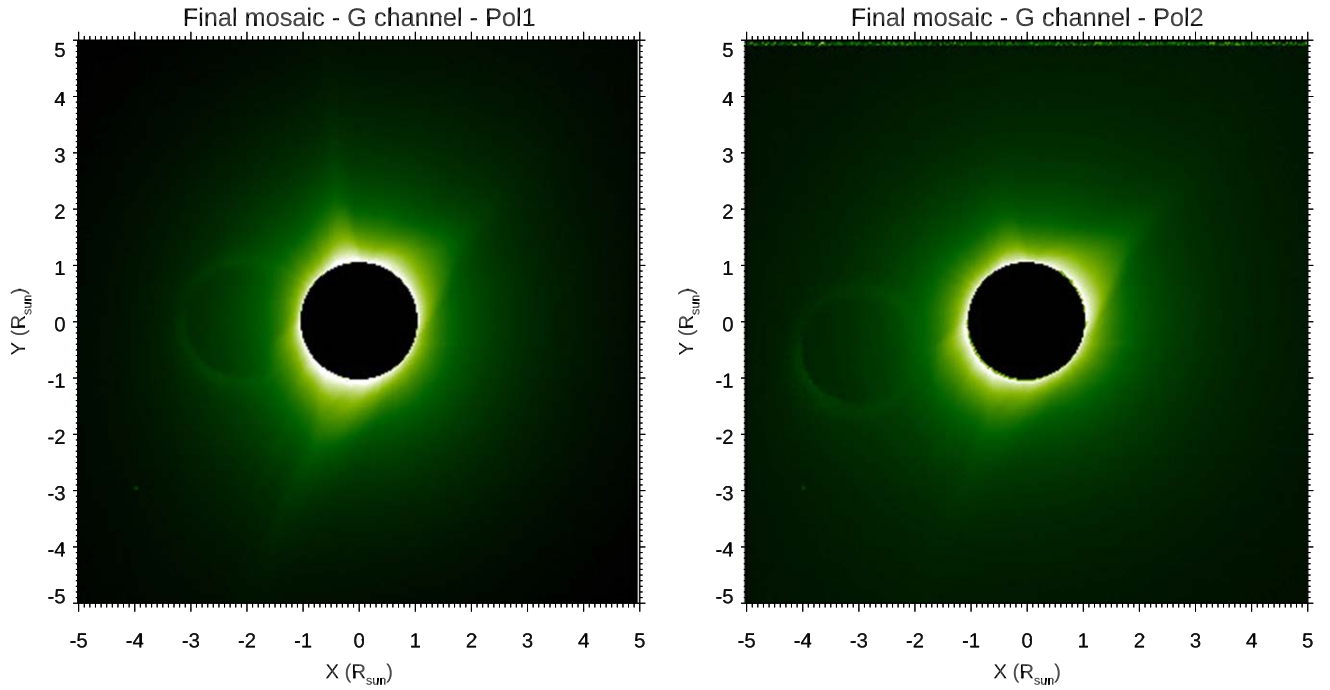


**Figure 10.** Resulting mosaic images in the G channel constructed from the two sequences of 15 exposures acquired with the first (left) and the second (right) orientations of the linear polarizer. Both images show the presence of a ghost that is due to internal reflections by the linear polarizing filter.

components are given by (see, e.g., Reginald et al. 2017)

$$I(i, j) = I_{pol2}(i, j) + I_{pol1}(i, j) \quad (3)$$

$$U(i, j) = I_{pol2}(i, j) - I_{pol1}(i, j) \quad (4)$$

$$Q(i, j) = U(i, j) / \tan 2\alpha(i, j). \quad (5)$$

Hence, the difference between the Pol1 and Pol2 images provides directly the  $U$  component of the Stokes vector, and this difference is zero around angles separated by  $90^\circ$ , leading to the polarization cross pattern shown in Figure 11 (top left panel).

### 5.1. Determination of the Phase Angle

Because (as mentioned above) the linear polarization vector in the solar corona is always tangent to the solar limb, the 2D distribution  $(i, j)$  of the angle  $\alpha(i, j)$  in the acquired images is easily determined once the position of the center of the Sun is well known. Nevertheless, the angle  $\alpha$  has to be corrected for a phase angle  $\phi$ , related to the reference angular orientation of the linear polarizer for instance with respect to the columns of images, which is in general unknown. In order to measure  $\phi$ , the normalized  $U_{norm}$  intensity image  $U_{norm} = (I_{pol2} - I_{pol1}) / (I_{pol2} + I_{pol1})$  [%] has been converted into polar coordinates, as shown in Figure 11 (top right panel). The latitudinal distributions of  $U_{norm}$  have been extracted only in the inner coronal regions (where the signal-to-noise ratio is higher) and fitted with a sinusoidal function, as is shown in Figure 11 (bottom panel). The resulting value of  $\phi = -75.3 \pm 0.3$  has been employed then to derive the 2D distribution of the angle  $2\alpha(i, j) = 2 \arctan Y(i, j) / X(i, j) + \phi$ , where the  $X$  and  $Y$  coordinates are the standard Cartesian coordinates in a reference system centered on the Sun.

### 5.2. Determination of the Degree of Linear Polarization

Once the 2D distribution of the  $\alpha$  angle is determined, Equations (1)–(5) provide directly a measurement of the

Stokes vector components  $[I, Q, U]$ , as well as the degree of linear polarization  $p$ ; the resulting 2D distributions of  $[I, Q, U]$  components are shown in Figure 12. The main problem with the analysis described here is that it is based on the combination only of two different images (Figure 10) acquired with two different orientations of the linear polarizer. This results in the relatively simple Equations (3)–(5), but these equations have two main disadvantages. First, the 2D distribution of angle  $\alpha$  has been determined with respect to the position of the center of the Sun, which is in general not known. As mentioned, for this TSE campaign, thanks to the presence of stars, the center of the Sun behind the lunar disk has been determined in the mosaic images, but this is not always possible. Second, having only two polarized images, the expression for the  $Q$  component (Equation (5)) has a tangent function in the denominator, and for pixels close to the angular positions where  $2\alpha = k90^\circ$  ( $k = 0, 1, 2, 3$ ), the expression for  $Q$  diverges, leading to unreliable values in the cross-like pattern visible in Figure 12 (bottom right panel).

For these reasons, measurements of  $p$  [%] in the solar corona are usually performed by acquiring at least three images with three different orientations of the linear polarizer. Unfortunately, as explained above (end of Section 3.3), the third and last sequence of polarized images acquired during this TSE is affected by light coming from the solar disk emerging behind the Moon at the end of totality, and these images have not been analyzed here. In any case, despite the above problems related to the use of only two polarized mosaic images, the 2D distribution of degree of linear polarization  $p$  was successfully determined, and this was done independently for the three RGB channels. The resulting  $p$  images (Figure 13, top panels) are affected by artifacts related to the reflection ghosts (Figure 10), and also by the mentioned cross-like pattern of diverging pixels. The resulting 2D distribution of  $p$  [%] appears to be well determined, at least in the inner coronal regions, and in good agreement with values provided for instance by Snik et al. (2020; see their

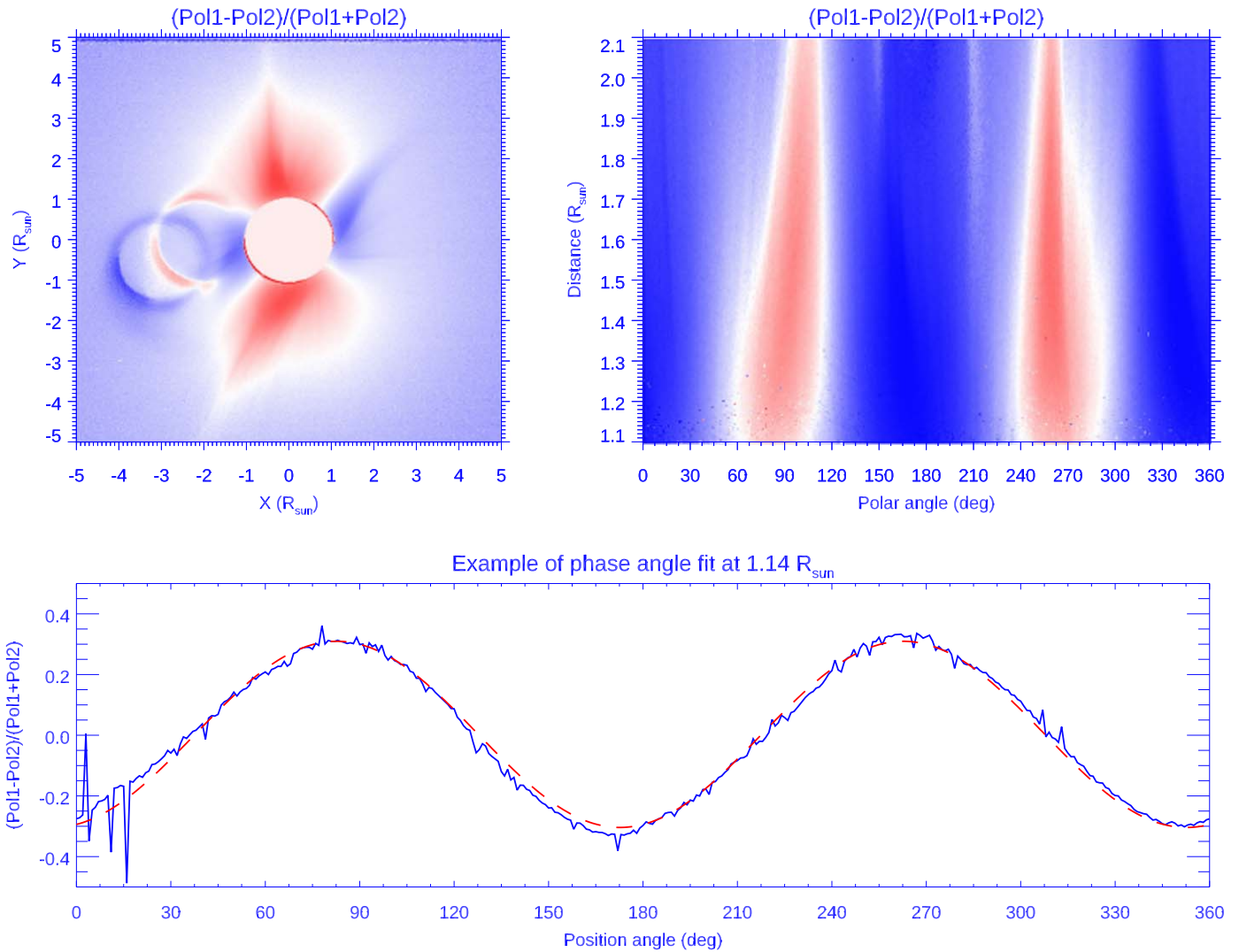


**Figure 11.** Top left: relative difference between the two mosaics in the G channel (Pol1 and Pol2) acquired with two different orientations of the linear polarizer separated by  $90^\circ$ . The color scale shows positive (negative) values plotted as red (blue) colors. Top right: the same image transformed into polar coordinates and showing the modulation of polarization between  $1.1$  and  $2.1 R_{Sun}$ . Bottom: latitudinal variation of intensity at constant altitude (solid line) and the corresponding sinusoidal fit (dashed line), plotted as a function of the position angle (running counterclockwise from the X-axis).

Figure 2). The orientation of the polar axis of the Sun in these images has been determined from a coalignment with images acquired by the Mauna Loa COSMO K-Coronagraph (see below).

In what follows I describe how the resulting  $p$  image in the G channel has been radiometrically calibrated to measure the polarized brightness  $pB$  and further analyzed to measure the 2D distribution of coronal electron densities.

### 6. Image Radiometric Calibrations

In order to derive the electron densities  $n_e$  [ $\text{cm}^{-3}$ ] from the observed coronal emission, it is necessary to convert the intensities into physical units, typically in mean solar brightness (MSB); this corresponds to performing the radiometric calibration of images. In this work, the radiometric calibration has been performed first with respect to another instrument providing calibrated intensities (relative calibration), and second by employing the observed total solar brightness and the brightness of visible stars (absolute calibrations).

#### 6.1. Relative Radiometric Calibration

The relative radiometric calibration has been performed by rescaling the values of polarized brightness  $pB = I p$  [DN/s] derived here to those measured by the Mauna Loa COSMO K-Coronagraph (K-Cor) in Hawaii [ $1/B_{Sun}$ ]. This telescope provides  $pB$  images in a field of view from  $1.05$  to  $3 R_{Sun}$  with  $5.64$  arcsec/pixels and a spatial resolution of  $11''29$ . For the intercalibration, I employed in particular the 2 min averaged Mauna Loa Solar Observatory (MLSO) image at 17:43:55 UT. Once the TSE and MLSO images are coaligned with the Sun center, the rotation angle to be applied to TSE images has been determined from a comparison between the latitudinal locations of fainter coronal features visible in filtered images (Figure 14, left panel). Then, the comparison between  $pB$  values provided the calibration factor  $K_G$  to convert  $pB$  measurements from TSE images (in units of DN/s) to  $pB$  measurements from MLSO (in units of  $1/B_{Sun}$ ); the resulting value of the calibration factor is  $K_G = 1.54 \times 10^{11} B_{Sun}$  DN/s.

The right-hand image in Figure 14 shows again the presence of reflection ghosts in TSE images (top left quadrant) and the

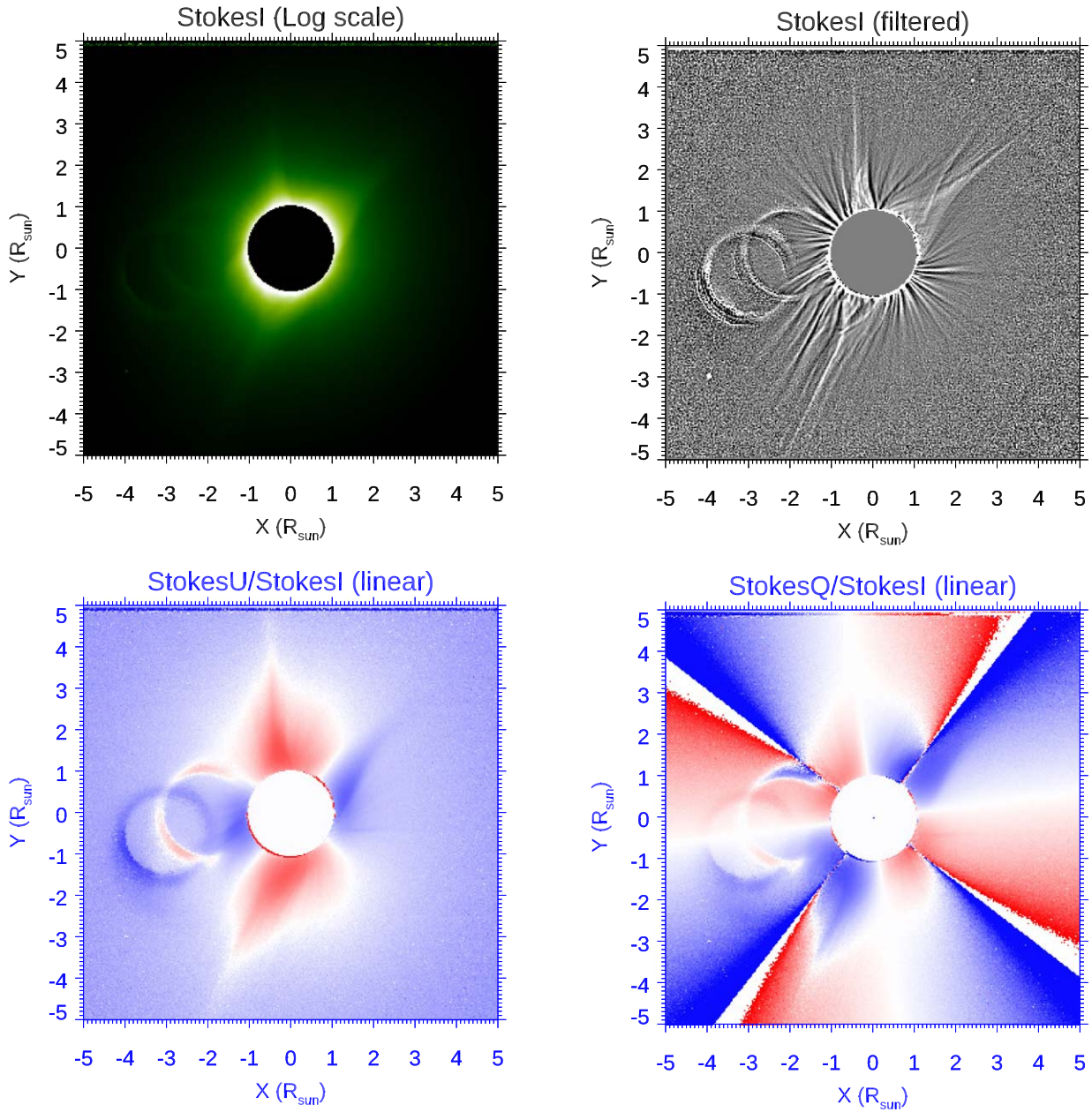


**Figure 12.** Top: 2D distribution of the Stokes vector  $I$  component plotted in log scale (left panel) and in linear scale after filtering (right panel). Bottom: the corresponding 2D distributions of the Stokes vector  $U$  (left panel) and  $Q$  (right panel) components plotted in linear scale after normalization over the  $I$  component. The top right image has been filtered by simply subtracting from the original image in log scale a median image obtained by replacing in each pixel with the average value over the surrounding area by  $(0.1 \times 0.1) R_{Sun}$ .

cross-like divergent pattern discussed above, but more importantly the comparison shows a really striking agreement between the TSE and MLSO values after rescaling with the above calibration factor, such that the boundary region between the two TSE and MLSO images (arbitrarily assumed at  $1.5 R_{Sun}$ ) is not even visible.

A more quantitative comparison between  $pB$  values measured here from TSE images and provided by MLSO is shown in Figure 15. These plots (providing the measured values without any smoothing of the data) show a very good agreement between  $pB$  values not only in their latitudinal distribution but also in their radial variations, an agreement that is comparable to, for instance, what was obtained by Judge et al. (2019) with a much more complex instrumentation. The bottom right panel of Figure 15 also shows that at  $2 R_{Sun}$  the

quality of  $pB$  measurements obtained with a DSLR camera during a TSE have a lower noise level than measurements obtained with the MLSO/COSMO coronagraph.

## 6.2. Absolute Radiometric Calibrations

More than just the relative radiometric calibration, the absolute radiometric calibration has also been determined here with two different methods. The first method is based on the measurement of the total brightness of the solar disk  $B_{Sun}$ ; given the full Sun images acquired before the beginning of the PSE, in principle this measurement is not difficult. The main problem is measuring the transmittance  $T$  of the Baader OD5.0 solar filter that was employed for the observations before the TSE. A transmittance curve as a function of wavelength is not

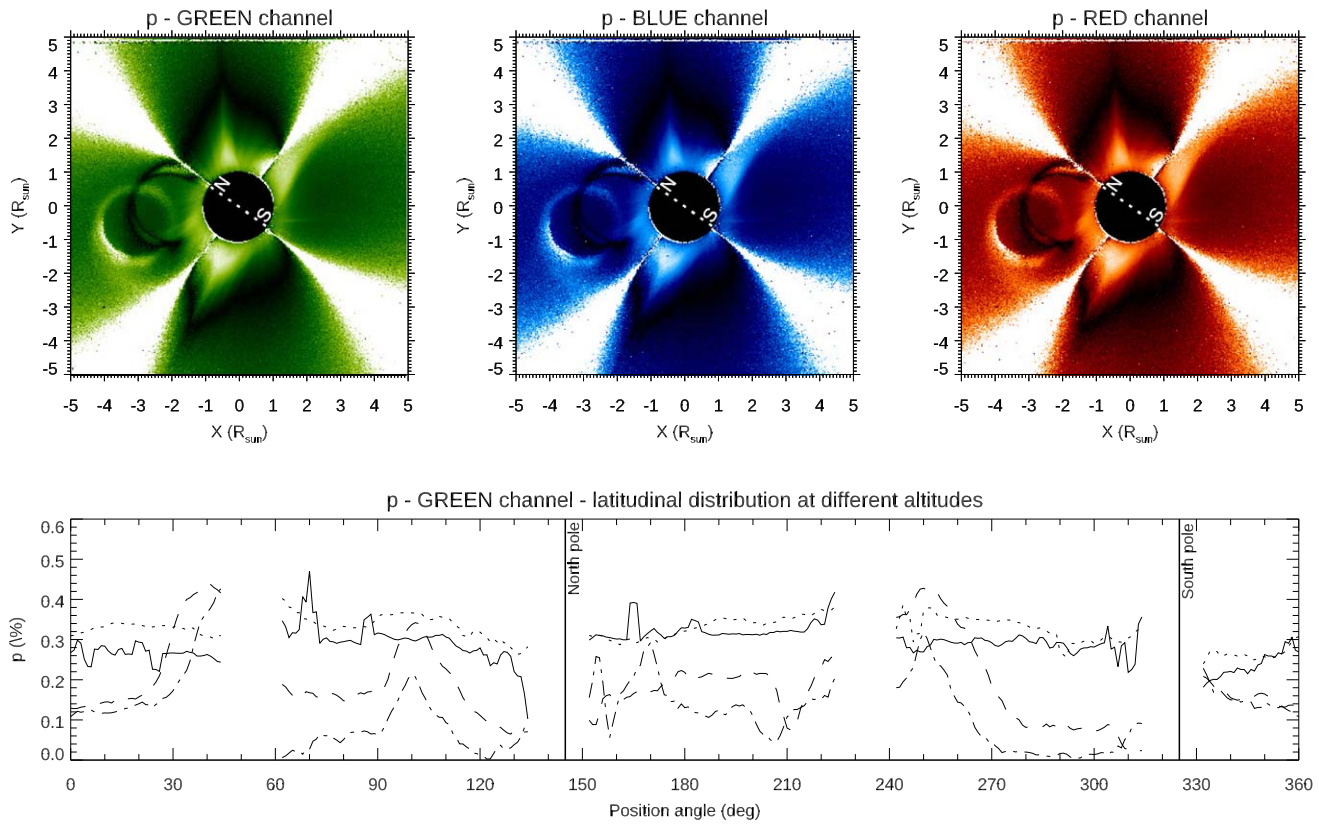


**Figure 13.** Top panels: degree of linear polarization  $p$  as derived from the green (left), blue (middle), and red (right) channels (linear color scales going from 0 to 0.5). The  $p$  distribution is affected by artifacts related to the reflection ghosts from the polarizing filter (left in each image), and also by the cross-like divergent pattern for angles where  $2\alpha = k 90^\circ$  (see text). The dotted line marks the polar axis of the Sun. Bottom: latitudinal distribution of  $p$  (counterclockwise from the  $X$ -axis) plotted at  $1.1 R_{sun}$  (solid line),  $1.2 R_{sun}$  (dotted line),  $2 R_{sun}$  (dashed line), and  $2.5 R_{sun}$  (dashed-dotted line); vertical lines marks the poles of the Sun. Values around the cross-like divergent pattern have been omitted in these plots.

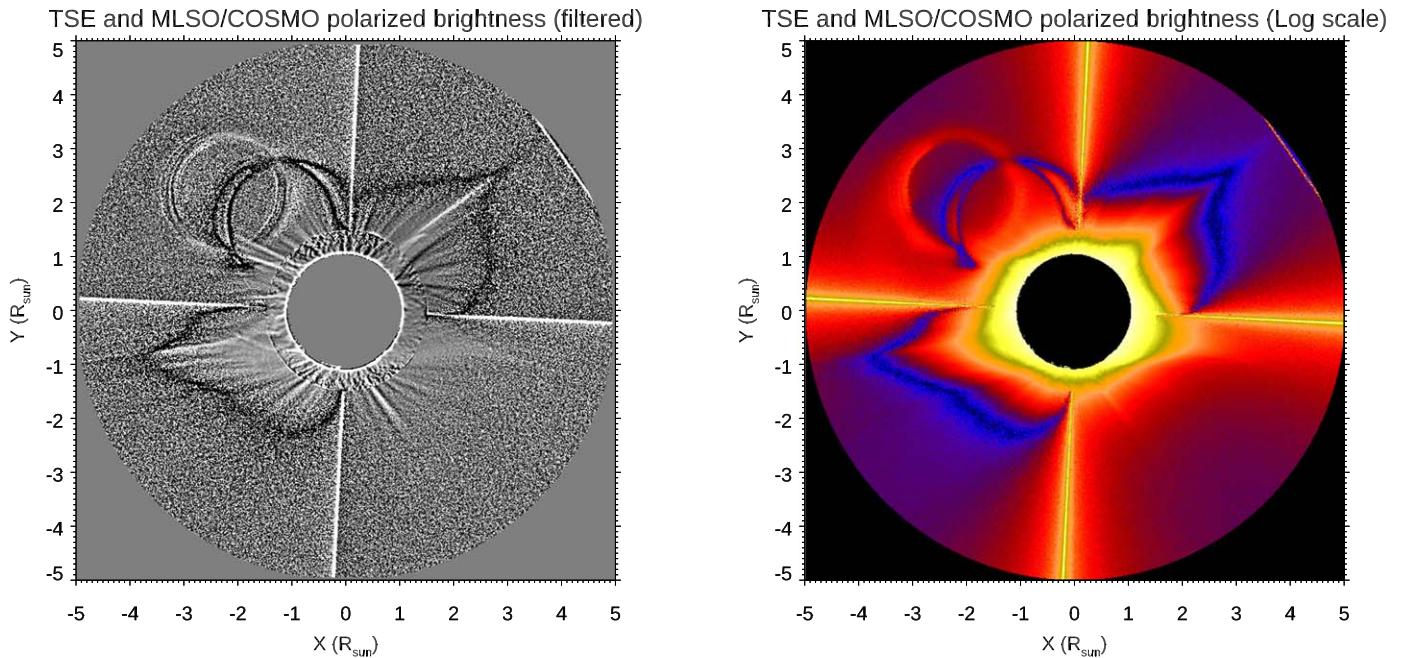


**Figure 14.** Combined images obtained from a superposition of  $pB$  values measured by MLSO/COSMO (shown in the range between 1 and  $1.5 R_{sun}$ ) and those measured in this work with TSE observations (shown in the range between  $1.5$  and  $5 R_{sun}$ ), after coalignment, rotation, and intercalibration with MSLO/COSMO values. The right image shows the  $pB [1/B_{sun}]$  plotted in log scale, while the left image shows the nice correspondence between the fainter coronal features after image filtering.

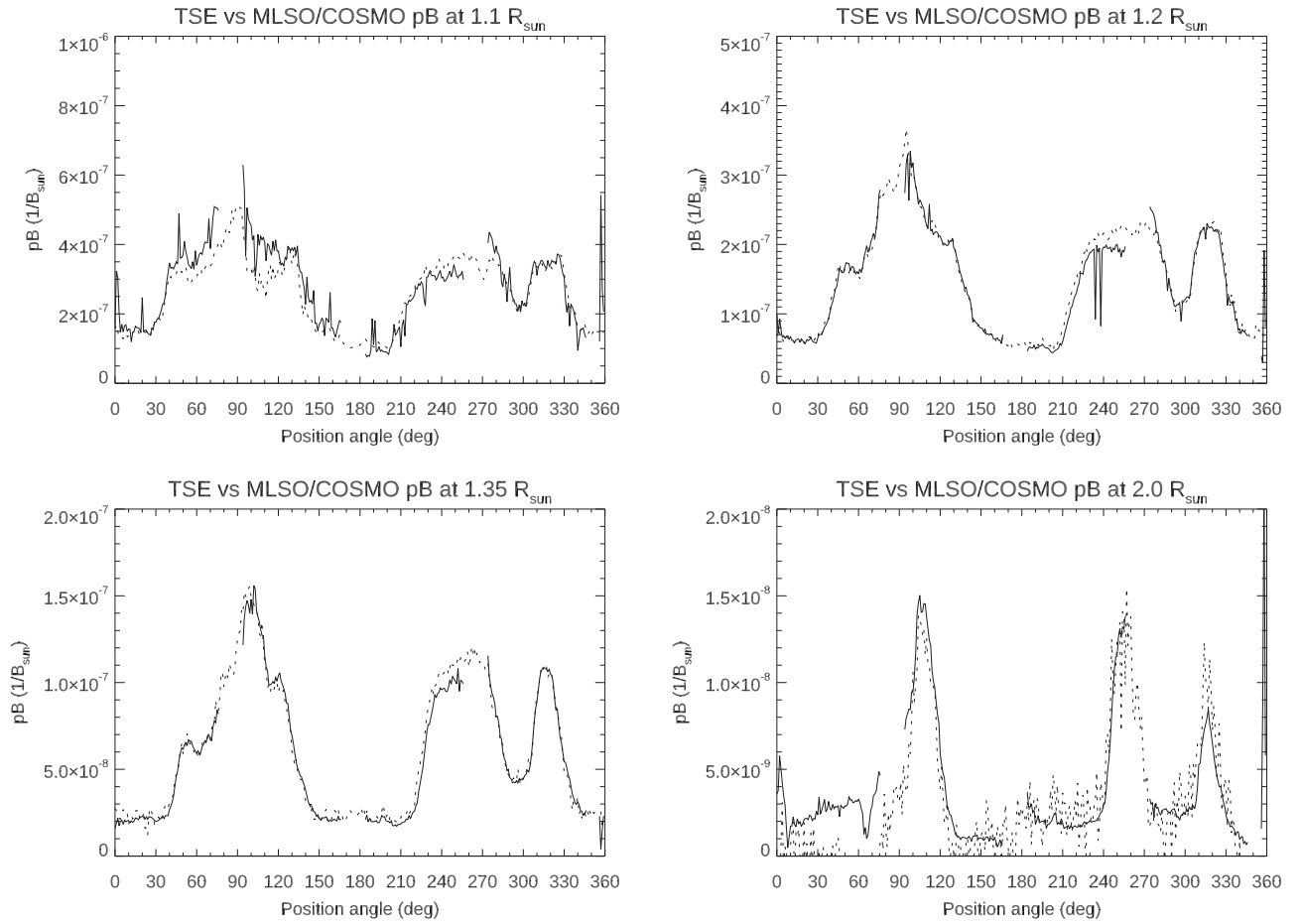


**Figure 15.** Comparisons between the latitudinal distribution of  $pB$  values measured here from TSE (solid lines) and provided by MLSO (dotted lines) at  $1.1 R_{Sun}$  (top left),  $1.2 R_{Sun}$  (top right),  $1.35 R_{Sun}$  (bottom left), and  $2.0 R_{Sun}$  (bottom right). Again, values around the cross-like divergent pattern have been omitted in these plots. No smoothing has been applied to the data; the bottom left panel is directly comparable with Figure 9 (bottom panel) by Judge et al. (2019).

provided by the manufacturer of this filter, but this was measured by Koukarine et al. (2013), who provided (their Figure 4) the measured transmittance curve. From this figure, the transmittance values  $T$  have been extracted and averaged over different wavelength intervals, obtaining a value for the transmittance in the G channel ( $T_G = 5.30 \times 10^{-6}$ ), as well as corresponding values for the R ( $T_R = 4.45 \times 10^{-6}$ ) and the B ( $T_B = 6.11 \times 10^{-6}$ ) channels.

The selected full Sun image has been then analyzed by repeating exactly the same steps explained above for the TSE images, and by separating the image into three RGB images. Finally, the MSB values  $B_{sun,G}$ ,  $B_{sun,R}$ , and  $B_{sun,B}$  [DN/(pix<sup>2</sup> s)] have been computed for each of the three RGB colors as (see Cox 2000)

$$B_{sun,RGB} = F_{RGB}/(\pi A_{RGB} T_{RGB} t_{exp}) \quad (6)$$

where  $F_{RGB} = I_{RGB} t_{exp}$  [DN] is the intensity flux obtained by integrating over the whole visible solar disk in each image,  $A_{RGB}$  [pix<sup>2</sup>] is the area covered by the solar disk in pixels,  $T_{RGB}$  are the transmittances given above, and  $t_{exp}$  [s] is the exposure time. The resulting values computed with the above formula are  $B_{G,sun} = 3.26 \times 10^{11}$  DN/(pix<sup>2</sup> s),  $B_{R,sun} = 3.56 \times 10^{11}$  DN/(pix<sup>2</sup> s), and  $B_{B,sun} = 3.06 \times 10^{11}$  DN/(pix<sup>2</sup> s), respectively, for the G, R, and B channels. In particular, the derived value of  $B_{sun,G}$  is about a factor of  $\sim 2$  larger than the normalization constant  $K_G$  determined with relative intercalibration to rescale

TSE measurements of  $pB$  to values provided by MLSO. The origin for this disagreement is not known, but considering the amateur equipment employed in this work, and the large uncertainties in particular in the measurement of Baader OD5.0 filter transmittance, such a disagreement can be considered as acceptable and not surprising.

The presence of visible stars in TSE images also provides an alternative method of determining the absolute radiometric calibration, based on the observed star intensities. In particular, from bidimensional Gaussian fitting of the  $\alpha$ -Leonis and  $\nu$ -Leonis stars observed in the G channel in the last four exposures acquired during the first TSE sequence, it turns out that the average intensities  $I_G$  [DN/s] for the two stars are  $I_{G,\alpha} = (3.64 \pm 0.05) \times 10^5$  DN/s and  $I_{G,\nu} = (1.1 \pm 0.1) \times 10^4$  DN/s. This corresponds to an observed magnitude difference  $\Delta m_{G,obs} = -2.5 \log_{10}(I_{G,\nu}/I_{G,\alpha}) = 3.80$ . This is in very good agreement with the known visual magnitude difference  $\Delta m = m_\nu - m_\alpha = 5.15 - 1.35 = 3.80$  as provided by Stellarium (based on the Naval Observatory Merged Astrometric Dataset, or NOMAD; see Zacharias et al. 2004), including atmospheric extinction. This also suggests that intensities measured in the G channel represent to a first approximation the intensities of stars in the V-band. On the other hand, the total intensity of the corona, summing in the observed sky region between  $\pm 5 R_{Sun}$  both in X and Y coordinates, is  $I_{G,cor} = 3.77 \times 10^{10}$  DN/s, corresponding to a total magnitude of the solar corona in

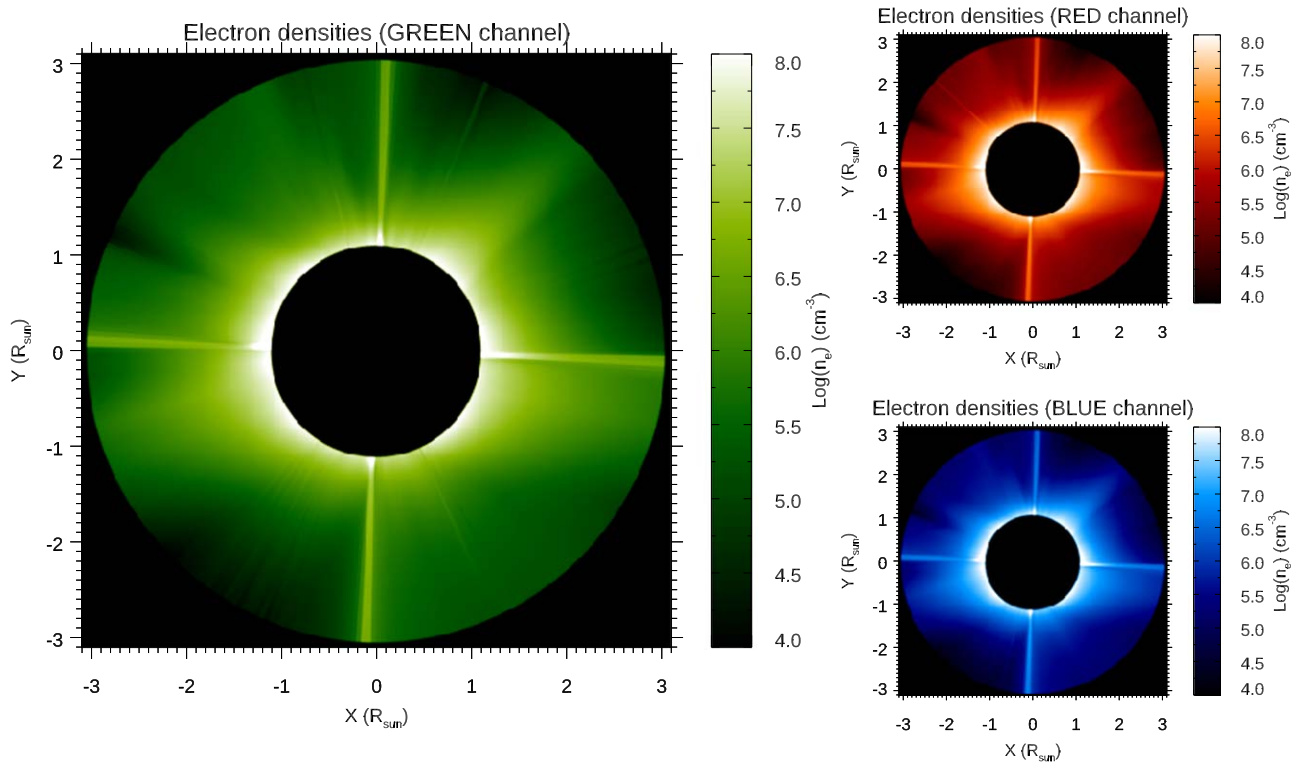


**Figure 16.** Electron density maps as derived from the inversion of  $pB$  maps obtained with three different pixel colors, and in particular for the green (left), red (top right), and blue (bottom right) pixels.

the G channel (close to the V-band) of  $m_{G,cor} = m_{G,\alpha} - 2.5 \log_{10}(I_{G,cor}/I_{G,\alpha}) = -11.19$ . This can be compared with the Moon visual apparent magnitude  $m_{moon} = -12.73$  (Cox 2000) and implies that the observed solar corona was approximately a factor of  $\sim 4$  dimmer than the full Moon.

The above measurements can also be employed to derive another estimate for the intensity of the full Sun  $I_{G,sun}$  [DN/s], and hence for the value of MSB, thus providing another method for the absolute calibration. Starting from the known apparent visual magnitude of the Sun  $m_{sun} = -26.75$  (Cox 2000), and given the above total intensity and magnitude of the corona, the corresponding intensity [DN/s] of the full Sun is given by

$$I_{G,sun} = I_{G,cor} \cdot 10^{(m_{G,cor} - m_{G,sun})/2.5}, \quad (7)$$

which can be converted into  $B_{G,sun} = I_{G,sun}/A_G = 2.99 \times 10^{11}$  DN/(pix<sup>2</sup> s). In the above estimates, it is assumed (as suggested by the agreement between the known visual magnitude difference and observed intensity ratio for  $\alpha$ -Leo and  $\nu$ -Leo in the G channel) that the known visual magnitudes for stars and the Sun correspond to the intensity fluxes measured here from the G channel. The above value is quite close to the MSB value measured independently with the full Sun disk image of  $B_{G,sun} = 3.26 \times 10^{11}$  DN/(pix<sup>2</sup> s), and is again approximately a factor of  $\sim 2$  larger than the normalization constant needed to rescale TSE measurements to values provided by MLSO. The reason for this disagreement is not known, but for this second measurement, possible calibration errors cannot be ascribed to uncertainties in the transmittance of the Baader OD5.0 solar filter employed for the first measurement. Because the above two absolute calibration methods are independent, and because the resulting disagreement with respect to absolute  $pB$  values provided by MLSO is about the same, this suggests the

possible existence of a systematic error in the measurements derived here from TSE images, whose origin is unknown.

## 7. Derivation of Electron Densities

Once the  $pB$  images are calibrated in standard units, the resulting values can be fitted radially to derive radial profiles of the coronal electron density  $n_e$ . This has been done here with the standard Van de Hulst inversion technique (van de Hulst 1950). This well-established method, assuming a simple, spherically symmetric corona at each latitude, has been more recently validated by making a comparison with tomographic electron density reconstructions (Wang & Davila 2014).

The resulting 2D electron density maps as obtained with  $pB$  images for the three RGB channels are shown in Figure 16. These maps were obtained starting from  $pB$  measurements derived with TSE images and after relative radiometric calibration to rescale the observed values to those provided by MLSO in standard units of MSB. Because the absolute radiometric calibrations derived here with the full Sun image and with stars give values of MSB a factor of  $\sim 2$  larger, these higher MSB values would simply reduce the  $pB$ , and thus the resulting densities, exactly by the same factor.

A more quantitative comparison is provided in Figure 17, showing the electron density values derived here between 1.1 and 3  $R_{Sun}$  in the two brighter coronal streamers (dashed red lines) visible in the top right and bottom left quadrants in Figure 16, and in the nearby polar coronal holes (solid blue lines). Figure 17 also shows that the density profiles from TSE images have a very good agreement with reference values provided for instance by Gibson et al. (1999) for minimum coronal streamers (thicker orange dashed line), and with values provided by Cranmer et al. (1999) and Guhathakurta et al. (1999) for coronal holes (thicker cyan solid lines).

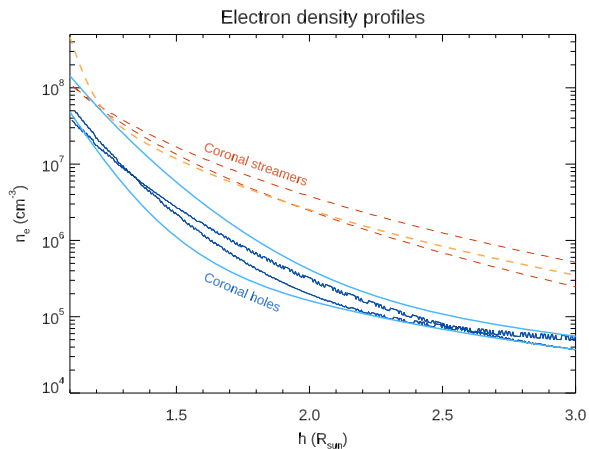


**Figure 17.** Electron density radial profiles plotted along coronal streamers (dashed red lines) and coronal holes (solid blue lines); the measured profiles are compared here with standard reference profiles given by Gibson et al. (1999) for minimum coronal streamers (thicker orange dashed line) and by Cranmer et al. (1999) and Guhathakurta et al. (1999) for coronal holes (thicker cyan solid lines).

## 8. Summary and Conclusions

In this work I analyzed the sequence of images acquired during the total solar eclipse of 2017 August 21 from the Idaho Falls area. The images were acquired with a standard DSLR camera mounted on a simple fixed tripod and equipped with a cost-effective zoom and linear polarizing filter. After demosaicking to separate pixels into the three RGB colors of the Bayer filter matrix, the images (having a projected pixel size of  $3''.7$ ) were corrected for the dark currents and flat field, and then coaligned based on the detected position of the brighter star  $\alpha$ -Leonis. From bi-Gaussian fitting of the star intensity distribution, it turns out that the images have an effective resolution of about  $10''$ , comparable with the apparent sky motion in 1 s.

After image coalignment, each sequence of bracketing images has been combined by measuring the intensity for each pixel in the interval of linearity of the detector response as a function of the exposure time. This provided one mosaic image for each one of the three RGB colors: one triplet without a polarizer, and the second and third ones with a linear polarizer. Comparisons among radial intensity profiles obtained with pixels corresponding to different colors, and hence located in different positions in the RGB Bayer filter matrix of the DSLR camera, show considerable (up to  $\sim 5\%$ – $10\%$ ) relative intensity differences in the inner coronal regions (below  $\sim 1.5 R_{Sun}$ ). This means that even small differences in the projected altitudes of nearby pixels in the camera ( $3''.7$ , corresponding to  $3.9 \times 10^{-3} R_{Sun}$ ) result in considerable relative intensity differences in the observed corona. This may partially affect the measurements of degree of linear polarization as obtained from a combination of intensities observed in nearby pixels with different orientations of linear polarizers by assuming that the different pixels are sampling the same corona, as done in the analysis of images acquired with a PolarCam (e.g., Reginald et al. 2017; Judge et al. 2019; Fineschi et al. 2019). In principle, images acquired with PolarCams should be analyzed instead with methods similar to those developed by many authors for debayering or demosaicking regular RGB images acquired by DSLR cameras (e.g., Ramanath et al. 2002; Parmar et al. 2005), in particular if one wants to exploit these images to resolve fine features located in the inner corona.

In this work, the mosaic images acquired with different polarizations have been combined to measure the degree of linear polarization  $p$  [%] and the three components [ $I$ ,  $Q$ ,  $U$ ] of the Stokes vector. Despite the presence of a few artifacts (ghosts due to reflections from the polarizing filter, and a cross-like divergent pattern where solutions for the  $Q$  component of the Stokes vector diverge), the resulting values of  $p$  are in nice agreement with those provided for instance by Snik et al. (2020) for the same TSE. Relative radiometric calibration has been performed by rescaling measurements of polarized brightness  $pB$  obtained here from the TSE with those provided by the Mauna Loa K-Cor coronagraph at MLSO, showing a very good agreement both in the latitudinal distribution and at different altitudes up to  $2 R_{Sun}$ , with very good signal-to-noise ratio.

Absolute radiometric calibrations of  $pB$  images have been performed as well, with two different methods: by measuring the full-disk mean solar brightness with one image acquired before the partial eclipse with an OD5.0 filter, and by measuring the brightness of the  $\alpha$ -Leo and  $\nu$ -Leo stars visible in the eclipse images. Both methods provided values of MSB approximately a factor of  $\sim 2$  larger than what was derived from intercalibration with MLSO  $pB$  measurements, resulting in coronal densities lower by a factor of  $\sim 2$  than what could be derived from MLSO calibrated images. The reason for this systematic disagreement is unknown. It is curious to notice here that a similar systematic disagreement by about a factor of  $\sim 2$  was recently found also by Lamy et al. (2019), from a comparison between the  $pB$  values measured by MLSO and the Large Angle and Spectrometric Coronagraph Experiment (LASCO) on the one hand, and those predicted from MHD numerical simulations on the other hand (see their Figure 23, left panels), with MLSO  $pB$  values higher again than those predicted by MHD simulation, something that these authors ascribed to the possible uncertainties in coronal abundances, affecting the radiative loss function. Finally,  $pB$  measurements have been employed here to derive an electron density image, and the resulting values are in agreement with those measured by previous authors in coronal streamers (Gibson et al. 1999) and coronal holes (Cranmer et al. 1999; Guhathakurta et al. 1999). This is the first published map of coronal electron density measurements for the 2017 August 21 TSE.

In summary, this work demonstrates that images acquired during a TSE with cost-effective amateur equipment can provide high-quality images that can be employed for scientific analysis purposes. In the aim of the author, this work will hopefully inspire and motivate future amateur astronomers and educators to create projects based on similar images acquired with DSLR cameras during TSEs, for instance in the occasion of the forthcoming eclipse on 2024 April 8 that will again cross the United States and will last more than 4 minutes.

The author thanks L. Abbo and C. Benna for their invaluable help and support in the organization of the observational campaign, making this work possible. The author also thanks the anonymous referee for useful suggestions.

## References

- Axelsen, R. A. 2017, JAVSO, 45, 92
- Banyś, T. A. J., & Kata, M. 2014, Gerb, 6, 81
- Bemporad, A., Abbo, L., & Benna, C. 2017, The 2017 Great American Eclipse: first report on the observational campaign, Istituto Nazionale di Astrofisica Technical Report, 177, <http://hdl.handle.net/20.500.12386/684>

- Bemporad, A., Baccani, C., Capobianco, G., et al. 2015, in Society of Photo-Optical Instrumentation Engineers (SPIE) Conf. Ser., 9604, Solar Physics and Space Weather Instrumentation VI, 96040C
- Boe, B., Habbal, S., Druckmüller, M., et al. 2020, *ApJ*, 888, 100
- Burkepile, J., Boll, A., Casini, R., et al. 2017, *AGUFM*, 2017, SH13B–2477
- Cheng, S., & Cheng, S. 2011, *JIMO*, 39, 39
- Collins, D. F. 2013, *JAVSO*, 41, 391
- Collins, D. F., & Prasai, A. 2009, *SASS*, 28, 121
- Cox, A. N. 2000, *Allen's Astrophysical Quantities* (New York: AIP)
- Cranmer, S. R., Kohl, J. L., Noci, G., et al. 1999, *ApJ*, 511, 481
- DeForest, C. E., Howard, R. A., Velli, M., Viall, N., & Vourlidas, A. 2018, *ApJ*, 862, 18
- Deshmukh, S. 2015, *JAVSO*, 43, 172
- Di Giovanni, G. 2016, *JBAA*, 126, 79
- Dodson, J. B., Robles, M. C., Taylor, J. E., DeFontes, C. C., & Weaver, K. L. 2019, *JApMC*, 58, 2363
- Druckmüller, M., Rušin, V., & Minarovjech, M. 2006, *CoSka*, 36, 131
- Fiacconi, D., & Tinelli, L. 2009, *OEJV*, 114, 1
- Filippov, B., Koutchmy, S., & Lefaudeux, N. 2020, *SoPh*, 295, 24
- Fineschi, S., Capobianco, G., Massone, G., et al. 2019, *NCimC*, 42, 26
- Frissell, N. A., Katz, J. D., Gunning, S. W., et al. 2018, *GeoRL*, 45, 4665
- Gibson, S. E., Fludra, A., Bagenal, F., et al. 1999, *JGR*, 104, 9691
- Gopalswamy, N., & Gong, Q. 2018, *Proc. SPIE*, 10769, 107690X
- Gopalswamy, N., Yashiro, S., Reginald, N., et al. 2018, AAS Meeting 231, 220.08
- Guhathakurta, M., Fludra, A., Gibson, S. E., Biesecker, D., & Fisher, R. 1999, *JGR*, 104, 9801
- Hanaoka, Y., Hasuo, R., Hirose, T., et al. 2018, *ApJ*, 860, 142
- Hoot, J. E. 2007, *SASS*, 26, 67
- Hoot, J. E. 2012, *SASS*, 31, 191
- Hudson, H., Bender, M., Collier, B., et al. 2018, AAS Meeting 231, 220.03
- Hudson, H. S., McIntosh, S. W., Habbal, S. R., Pasachoff, J. M., & Peticolas, L. 2011, arXiv:1108.3486
- Jang, S.-J., & Song, I.-O. 2015, *PKAS*, 30, 765
- Jejčić, S., & Heinzel, P. 2009, *SoPh*, 254, 89
- Jejčić, S., Heinzel, P., Zapiór, M., et al. 2014, *SoPh*, 289, 2487
- Judge, P., Tomczyk, S., Hannigan, J., & Sewell, S. 2019, *ApJ*, 877, 10
- Kloppenborg, B. K., Pieri, R., Eggenstein, H. B., Maravelias, G., & Pearson, T. 2012, *JAVSO*, 40, 815
- Koukarine, A., Nesterenko, I., Petrunin, Y., & Shiltsev, V. 2013, *SoSyR*, 47, 487
- Koutchmy, O., Koutchmy, S., Nitschelm, C., Sykora, J., & Smartt, R. N. 1988, in *Solar and Stellar Coronal Structure and Dynamics*, ed. R. C. Altrock, 256
- Koutchmy, S., Baudin, F., Abdi, S., Golub, L., & Sèvre, F. 2019, *A&A*, 632, A86
- Lamy, P., Floyd, O., Mikić, Z., & Riley, P. 2019, *SoPh*, 294, 162
- Littlefield, C. 2010, *JAVSO*, 38, 212
- Loughney, D. 2010, *JBAA*, 120, 157
- Madsen, C. A., Samra, J. E., Del Zanna, G., & DeLuca, E. E. 2019, *ApJ*, 880, 102
- Mikić, Z., Downs, C., Linker, J. A., et al. 2018, *NatAs*, 2, 913
- Miller, M. 2015, *SASS*, 34, 203
- Morgan, H., Habbal, S. R., & Woo, R. 2006, *SoPh*, 236, 263
- Nandy, D., Bhowmik, P., Yeates, A. R., et al. 2018, *ApJ*, 853, 72
- Nesci, R., Dalcer, D., Falasca, V., Moretti, A., & Panitti, U. 2020, *AsUAI*, 2, 10
- Parmar, M., Reeves, S. J., & Denney, T. S. J. 2005, *Proc. SPIE*, 5674, 259
- Pasachoff, J. M. 2017, *NatAs*, 1, 0190
- Pasachoff, J. M., Lockwood, C., Meadors, E., et al. 2018, *FrASS*, 5, 37
- Pasachoff, J. M., Rušin, V., Druckmüller, M., & Saniga, M. 2007, *ApJ*, 665, 824
- Páta, P., Fliegel, K., Klíma, M., Blažek, M., & Řeřábek, M. 2010, *Proc. SPIE*, 7798, 77982H
- Penn, M. J., Baer, R., Walter, D., et al. 2020, *PASP*, 132, 014201
- Peticolas, L., Hudson, H., Johnson, C., et al. 2019, in *ASP Conf. Ser.*, 516, Celebrating the 2017 Great American Eclipse: Lessons Learned from the Path of Totality, ed. S. R. Buxner, L. Shore, & J. B. Jensen (San Francisco, CA: ASP), 337
- Pieri, R. 2012, *JAVSO*, 40, 834
- Pyatnytskyy, M. Y. 2019, *OAP*, 32, 79
- Ramanath, R., Snyder, W. E., Bilbro, G. L., & Sander, W. A. 2002, *JEI*, 11, 306
- Reginald, N., Newmark, J., & Rastaetter, L. 2019, *SoPh*, 294, 100
- Reginald, N. L., Gopalswamy, N., Yashiro, S., Gong, Q., & Guhathakurta, M. 2017, *JATIS*, 3, 014001
- Reinisch, B. W., Dandenault, P. B., Galkin, I. A., Hamel, R., & Richards, P. G. 2018, *GeoRL*, 45, 1253
- Richards, T., Blackford, M., Butterworth, N., Crawford, G., & Jenkins, R. 2019, *OEJV*, 198, 1
- Rušin, V., Prikryl, P., & Prikryl, E. A. 2020, *MNRAS*, 495, 2170
- Samra, J. E., Judge, P. G., DeLuca, E. E., & Hannigan, J. W. 2018, *ApJL*, 856, L29
- Snik, F., Bos, S. P., Brackenhoff, S. A., et al. 2020, *ApOpt*, 59, F71
- Trillenber, P. 2019, *AmJPh*, 87, 839
- van de Hulst, H. C. 1950, *BAN*, 11, 135
- Vorobiev, D., Ninkov, Z., Bernard, L., & Brock, N. 2020, *PASP*, 132, 024202
- Walker, S., Butterworth, N., & Pearce, A. 2015, *JAVSO*, 43, 227
- Wang, T., & Davila, J. M. 2014, *SoPh*, 289, 3723
- Zacharias, N., Monet, D. G., Levine, S. E., et al. 2004, *BAAS*, 36, 1418
- Zhang, M., Bakos, G. Á, Penev, K., et al. 2016, *PASP*, 128, 035001